*energies*

MDPI

*Article*

# Common-Mode Choke Design to Eliminate Electrostatic Discharge Machining Bearing Currents in Wide-Bandgap Inverter-Fed Motor Drives

**Mustafa Memon and Mohamed Diab ***

School of Mechanical, Electrical and Manufacturing Engineering, Loughborough University, Loughborough LE11 3TU, UK; m.memon@lboro.ac.uk
* Correspondence: m.diab@lboro.ac.uk

**Abstract**

The electrification of mobility sectors, including automotive, aerospace, and robotics, has accelerated the need for compact and high-efficiency power converters in electric motor drives. Wide-bandgap (WBG) semiconductor–based inverters offer significant advantages over conventional silicon IGBT inverters by enabling higher switching speeds, elevated switching frequencies, and improved power conversion efficiency. However, the adoption of high-frequency switching introduces several challenges, particularly increased motor neutral point voltage stress, originating from inverter common-mode (CM) voltage. The increased neutral point voltage directly elevates motor bearing voltage, the primary driver of motor bearing currents, among which electrostatic discharge machining (EDM) bearing current is the primary cause of bearing degradation in low-power motors. This paper experimentally investigates the root causes of the EDM phenomenon and identifies the key factors influencing its occurrence and severity in WBG-based drive systems. The conventional CM choke designs effectively attenuate motor CM currents and EMI; however, they are ineffective in suppressing EDM bearing currents. In this paper, an alternative CM choke design methodology is proposed to eliminate EDM bearing currents by optimizing the choke inductance to shift the motor CM antiresonance frequency below the inverter switching frequency, thereby ensuring that nearly all source CM voltage is absorbed by the choke. This design approach effectively minimizes the voltage appearing at the motor neutral point and across the bearings, thereby suppressing EDM bearing current spikes without affecting motor DM performance. The choke parameters are mathematically derived for optimal performance and validated through experimental testing on a 2.2 kW three-phase star-connected induction motor powered by a wide-bandgap two-level voltage-source inverter.

**Keywords:** antiresonance frequency; common-mode choke; common-mode voltage; electrostatic discharge machining bearing current; motor drives; neutral-to-ground voltage; variable speed drives; wide-bandgap devices

check for updates

Academic Editors: Tao Wang, Chenwen Cheng and Yang Xiao

Received: 21 September 2025
Revised: 18 October 2025
Accepted: 29 October 2025
Published: 4 November 2025

**Citation:** Memon, M.; Diab, M. Common-Mode Choke Design to Eliminate Electrostatic Discharge Machining Bearing Currents in Wide-Bandgap Inverter-Fed Motor Drives. *Energies* **2025**, *18*, 5804. https://doi.org/10.3390/en18215804

**Copyright:** © 2025 by the authors. Licensee MDPI, Basel, Switzerland. This article is an open access article distributed under the terms and conditions of the Creative Commons Attribution (CC BY) license (https://creativecommons.org/licenses/by/4.0/).

## 1. Introduction

The past decade has witnessed a paradigm shift in the transportation and mobility sectors, primarily driven by stringent greenhouse gas emission regulations and rapid advancements in battery technologies. The resultant decrease in battery manufacturing costs has enabled widespread adoption of electric propulsion systems across industries

such as automotive, aerospace, and advanced robotics. This transformation has created a pressing need for compact, lightweight, and energy-efficient power electronic converters, which are central to the operation of electric motor drives.

In mobile platforms, reducing the size and weight of motor drives is not merely a design preference but a crucial factor in system-level efficiency. Lower power losses directly translate to reduced energy drawn from the battery pack, enabling downsizing of the battery itself. Such cascading benefits—lighter battery packs reducing total vehicle mass and, in turn, lowering energy consumption—underscore the strategic importance of highly efficient motor drive systems.

Recent advances in semiconductor technology have positioned WBG devices, particularly SiC and GaN, as transformative solutions for next-generation power converters [1]. Compared to traditional silicon switches, WBG devices exhibit superior material characteristics, including higher breakdown voltages, elevated thermal conductivity, and the ability to operate at significantly higher switching frequencies. These attributes enable drastic reductions in conduction and switching losses, increased power density, and the use of smaller passive components, which collectively enhance drive performance in weight-sensitive applications [2]. A notable example is the use of SiC MOSFETs in the powertrain of Tesla Model 3 electric vehicle, which achieves an estimated 2–3% improvement in inverter efficiency while significantly reducing system weight to approximately 4.8 kg—less than half that of similar silicon-based inverters [3].

Despite these advantages, the deployment of WBG devices introduces nontrivial challenges that must be addressed to ensure reliable long-term operation. The ultra-fast switching transitions inherent to SiC and GaN transistors produce steep voltage slew rates (high dv/dt), which intensify electromagnetic interference (EMI) and introduce complex insulation stress mechanisms within electric machines. In systems employing inverter-motor power cables, traveling wave reflections can lead to terminal overvoltage that may approach or even exceed twice the applied dc-link voltage [4]. These repetitive overvoltages accelerate the partial discharge phenomenon and degrade stator winding insulation, significantly shortening motor lifetime.

Moreover, high dv/dt CM voltage generated by WBG inverters contributes to the overvoltage appearing at the motor stator neutral point. The latest research in [5,6] indicates that motor neutral point overvoltage can pose greater risks than motor terminal overvoltage to motor windings as well as bearings, which in turn leads to premature motor failure. Motor neutral point overvoltage is caused by the propagation of inverter CM voltage through machine windings. Since the motor neutral point is typically floating, the CM voltage encounters an infinite impedance at the neutral point (due to a very small winding-to-frame parasitic capacitance), where the impedance mismatch between the motor surge impedance and the neutral point parasitic capacitive reactance results in overvoltage oscillations at the motor neutral point, a phenomenon known as the reflected wave effect [5]. It is pertinent to note that the motor neutral point overvoltage oscillations are characterized by the 1st antiresonance frequency of the motor, which is solely the function of machine CM winding inductance and its parasitic capacitances. Hence, the neutral point overvoltage, unlike motor terminal overvoltage, is independent of the cable length where this type of overvoltage can be observed without any cable connected between the inverter and motor [5]. Given that the 1st antiresonance frequency of the motor typically falls within the kHz range [6], the use of high-frequency WBG devices can enable the drive switching frequency or its harmonics to coincide with the motor 1st antiresonance frequency. Unlike inverter CM voltage, the magnitude of motor neutral point voltage is influenced by the relationship between drive switching frequency and machine antiresonance frequency. As the switching frequency approaches the machine antiresonance frequency, the neutral point

voltage increases. Furthermore, if both frequencies align, the overvoltage can increase significantly, exceeding CM voltage by several times due to motor resonance excitation [6].

This resonance effect is typically negligible with conventional silicon IGBT inverters, as their switching frequency is practically limited to 20 kHz, while motor antiresonance frequency is usually above 40 kHz [7]. However, with the rise of WBG devices, switching frequencies can now reach up to 200 kHz with SiC MOSFETs and even higher with GaN devices [8], increasing the likelihood of switching frequency or its harmonics matching the motor antiresonance frequency. As a result, an elevated neutral point voltage can impose considerable electrical stress on the winding turns closer to the stator neutral point, increasing the risk of insulation failure. Additionally, it directly affects the magnitude of bearing voltage, resulting in higher bearing current levels and accelerated bearing degradation.

CM chokes are widely utilized as a simple and highly effective approach to improve the motor drive performance by attenuating the CM noise and EMI in conventional variable speed drives. The conventional CM choke inductance is selected to create a high impedance in the CM current path within the desired frequency range, limiting the CM current flow to motor windings and frame. This ensures that CM current and EMI levels remain within the limits of safety standards. However, conventional choke designs have negligible impact on bearing current mitigation, as they do not address the fundamental causes of bearing currents, i.e., neutral point and bearing voltage. Figure 1 shows a typical motor drive system with the connection of a CM choke at the inverter terminals. It also demonstrates the CM current path and overvoltage oscillations between motor neutral point and grounded frame. In Figure 1, the two-level voltage-source inverter (VSI) supplies a three-phase star-connected motor through a four-core power cable. The three output terminals of the VSI (A, B, and C) are connected to the corresponding motor terminals (a, b, and c) through a CM choke and power cable, while the dc-link midpoint (O) is connected to the grounded motor frame (g). Since the CM current $I_{cm}$ flows in the same direction in all three phases, the CM fluxes add up in the choke core and provide a high impedance to $I_{cm}$, while allowing the line current to pass through with negligible impedance.

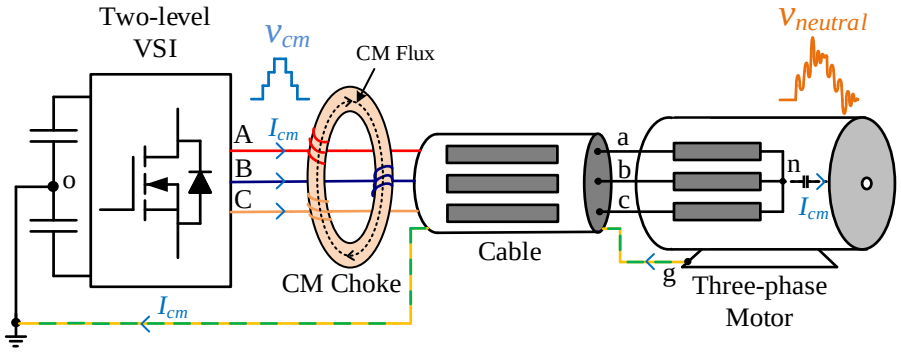



**Figure 1.** A typical motor drive with choke connected at inverter terminals.

While CM current and EMI mitigation remains important, studies have reported that 67% of motor failures are linked to bearing-related issues [9], resulting in costly repairs, operational downtime, and lost production in industries. This challenge has become even more critical with the increasing adoption of WBG inverter-fed motor drives in electric vehicles (EVs). In recent years, various motor bearing failures attributed to bearing voltages and EDM currents have been reported in EVs [10]. These failures contribute to bearing instability, excessive vibration, and noise, which not only degrade the performance but can also escalate into severe mechanical failures, posing significant reliability concerns for such advanced systems where the highest level of reliability is essential. Therefore, effective strategies to mitigate bearing currents are important to ensure the longevity and

reliability of wide-bandgap inverter-fed motor drives, particularly in critical applications such as EVs.

The conventional CM choke design to reduce the CM noise in variable-speed drives has been extensively studied in the literature for many years [11]. Various aspects of CM choke inductor design and performance have also been analyzed [12]. However, conventionally designed CM chokes are unable to mitigate motor neutral point voltage and corresponding bearing voltage and EDM bearing current. Experiments conducted in [13] evaluate the impact of different CM chokes on CM voltage and current, bearing voltage, and EDM bearing current. While the results confirm that CM chokes can reduce CM current by up to 90%, their influence on CM voltage, bearing voltage, and EDM current remains negligible. Additionally, in [14], various CM voltage mitigation techniques are evaluated, including the use of CM chokes. The analysis considers both the physical size and placement of the CM chokes within the motor drive system. The experimental results demonstrate that CM chokes are ineffective in reducing CM voltage, irrespective of their positioning.

EDM bearing current events are produced when the bearing voltage exceeds the dielectric breakdown threshold of the bearing lubricant. As the bearing voltage magnitude is predominantly governed by neutral point voltage, which in turn is largely driven by the inverter-generated CM voltage, it is worth exploring the CM voltage reduction techniques reported in the literature as potential solutions for mitigating EDM bearing currents. These include modified PWM schemes, modified inverter topologies, active noise cancellation circuits, soft switching inverters, and multilevel converters. The modified PWM strategies, such as active zero state PWM (AZSPWM) and near state PWM (NSPWM), reshape switching sequences to eliminate zero voltage vector generation [15–17], whereas modified inverter topologies commonly referred to as H7 and H8 architectures [18,19] or multilevel converters such as T-Type or neutral point clamped [20] inherently synthesize output voltages with reduced CM voltage through additional switching states and voltage levels, respectively. Furthermore, active noise cancellation circuits inject compensating voltages to counteract CM disturbances [21], while soft-switching inverters mitigate high dv/dt transitions, thereby lowering CM voltage excitation [22]. A summary of existing methods and their limitations is presented in Table 1.

**Table 1.** Existing And Proposed EDM Current Mitigation Methods and Their Limitations.

| Mitigation Method | Mechanism | EDM Current Effect | Cost/Complexity | Limitations |
|---|---|---|---|---|
| PWM schemes | Reduce CM voltage via modulation | Reduced | Low | Cannot eliminate EDM current across all conditions |
| Modified inverter topologies | Reduce switching stress and CM voltage | Reduced | Medium | Increased circuit complexity |
| Multilevel inverters | Lower dv/dt and CM voltage | Reduced | High | High cost; complex control |
| Sine wave/dv/dt filters/CM chokes | Smooth output voltage waveform and attenuate CM EMI | Unaffected | Medium | Ineffective for EDM current; increases losses |

It is worth noting that the aforementioned CM voltage reduction methods are limited in their ability to reduce the CM voltage to $\pm V_{dc}/6$ without having additional operational constraints. Although reducing the CM voltage by 66% can suppress the bearing currents,

EDM current spikes can still be observed due to the presence of overvoltage at the motor neutral point, especially when the switching frequency approaches the machine antiresonance frequency. Therefore, the CM voltage reduction methods may not be effective in eliminating the EDM current when applied to WBG inverters.

This paper proposes an alternate approach to design a CM choke for eliminating EDM bearing current. Since the added CM choke increases the inductance of the motor CM circuit, it is leveraged to shift the motor antiresonance frequency below the switching frequency to lower the voltage stress at the motor neutral point and bearings. Furthermore, by adjusting the ratio between antiresonance and switching frequency, motor bearing voltage can be reduced to a negligible value, thereby eliminating the EDM bearing current spikes. Additionally, the proposed CM choke design inherently reduces CM current magnitude and EMI by lowering the motor neutral point voltage, which serves as the primary source of CM currents. It is worth noting that the proposed CM choke only modifies the CM circuit of the motor, whereas the motor DM circuit remains unaffected. Design equations for selecting the optimal CM choke inductance and core are presented, while the effectiveness of the proposed strategy is validated through experimental testing on a 2.2 kW three-phase induction motor.

The contributions of this paper are as follows:

- Comprehensive explanation of non-linear behavior of bearing voltage and the corresponding EDM bearing current events in relation to drive switching frequency, offering deeper insight into the underlying mechanisms.
- Analysis of the limitation of conventional choke design approach.
- An alternative choke design approach to prevent the machine's antiresonance frequency from approaching or coinciding with the drive switching frequency, thereby avoiding the excitation of motor resonance that exacerbates bearing current.
- The proposed approach eliminates the EDM currents under all tested scenarios, regardless of switching frequency or dc-link voltage.
- Experimental evaluation of the proposed choke design approach against existing CM voltage reduction methods to highlight its superior performance.

The rest of the paper is structured as follows. Section 2 highlights the limitation of conventional CM choke design. Section 3 defines the bearing voltage and experimentally analyzes its influencing factors. In Section 4, the different types of bearing currents are demonstrated, while EDM bearing current and its influencing factors are experimentally elaborated. Section 5 presents the design equations for selecting CM choke inductance and core to eliminate EDM bearing current. Section 6 outlines the employed experimental approach in this work, detailing the methodologies used to evaluate the proposed choke design. Finally, Section 7 concludes the paper.

## 2. Limitation of Conventional CM Choke Design Approach

Conventional CM chokes are designed to offer large impedance to high-frequency CM currents. The inductance of the choke is selected based on the peak amplitude of the CM current harmonics and the desired level of attenuation, while its self-resonant frequency is chosen to be higher than the targeted harmonic frequencies for effective attenuation. However, these designs overlook motor neutral point voltage and its dependence on the relationship of motor CM antiresonance frequency and drive switching frequency. Since the added CM choke inductance can lower motor antiresonance frequency, it can bring the antiresonance frequency closer to or even match it with the drive switching frequency. This results in elevated motor neutral point voltage and corresponding bearing voltage and current.

### *2.1. Motor Neutral Point Voltage*

Motor neutral point voltage primarily stems from the CM voltage generated by power inverters in a motor drive system. The CM voltage is the average of the three pole voltages of the inverter relative to the dc-link midpoint. With conventional sinusoidal PWM, two-level VSIs yield four distinct CM voltage levels (i.e., $\pm V_{dc}/6$ and $\pm V_{dc}/2$), where $V_{dc}$ is the dc-link voltage. CM voltage pulses reflect at the stator neutral point due to impedance mismatch between winding surge impedance and motor neutral-to-frame impedance, causing voltage oscillations at the neutral point. This voltage increases with rising switching frequency and reaches its maximum when the switching frequency aligns with the machine antiresonance frequency. Beyond the antiresonance point, a further increase in switching frequency results in a reduction of the neutral point voltage.

This nonlinear behavior of motor neutral point voltage can be analyzed using the high-frequency CM equivalent circuit of the motor drive, as shown in Figure 2, where $V_{cm}$ and $L_e$ are the inverter CM voltage and motor winding inductance, respectively. As observed, motor neutral point voltage $V_{ng}$ is primarily capacitive in nature, as it is influenced by the capacitance between the neutral point and grounded frame, which is half of the motor winding-to-frame capacitance (i.e., $3C_{wf}/2$ ) ($\pi$-model), and the bearing voltage $V_b$ is observed across parallel combinations of rotor-to-frame and bearing capacitances. According to Figure 2, the bearing voltage, which is the primary cause of EDM bearing currents, is directly proportional to the neutral point voltage $V_{ng}$ rather than the inverter CM voltage, where it can be determined by the capacitive voltage divider circuit within the motor CM equivalent circuit. The bearing voltage can therefore be calculated by using the bearing voltage ratio (BVR) as follows:

$$\frac{V_b}{V_{ng}} = \frac{C_{wr}}{C_{wr} + C_{rf} + 2C_b} \tag{1}$$

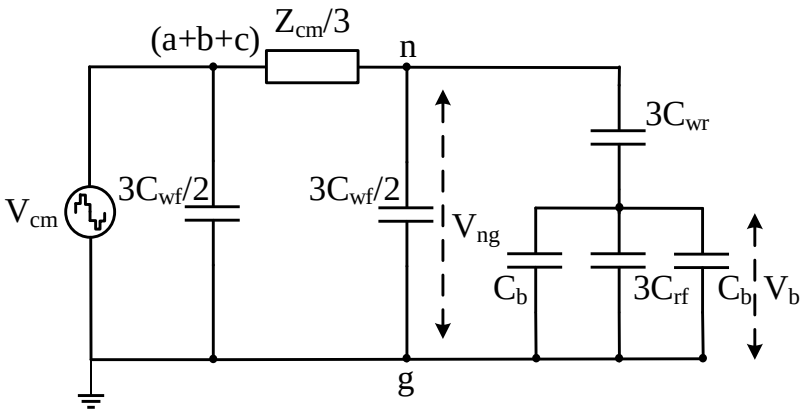



**Figure 2.** Motor CM equivalent circuit.

In a simple LC series circuit, the capacitive reactance and corresponding voltage exceed the inductive reactance and voltage when the supply frequency is below the circuit's antiresonance frequency and vice versa, as graphically demonstrated in Figure 3a, where the difference in both voltages is equal to the supply voltage, as shown in Figure 3b. Since the motor CM equivalent circuit behaves similarly, the neutral point voltage is higher than the CM inductive voltage when the drive switching frequency is below the motor antiresonance frequency. On the other hand, when the switching frequency exceeds the antiresonance frequency, the motor neutral point voltage becomes lower than the CM inductive voltage, while the difference between the two equals the CM voltage. Since

bearing voltage is a capacitive voltage divider of the neutral point voltage, it follows the same non-linear trend with switching frequency as the neutral point voltage.

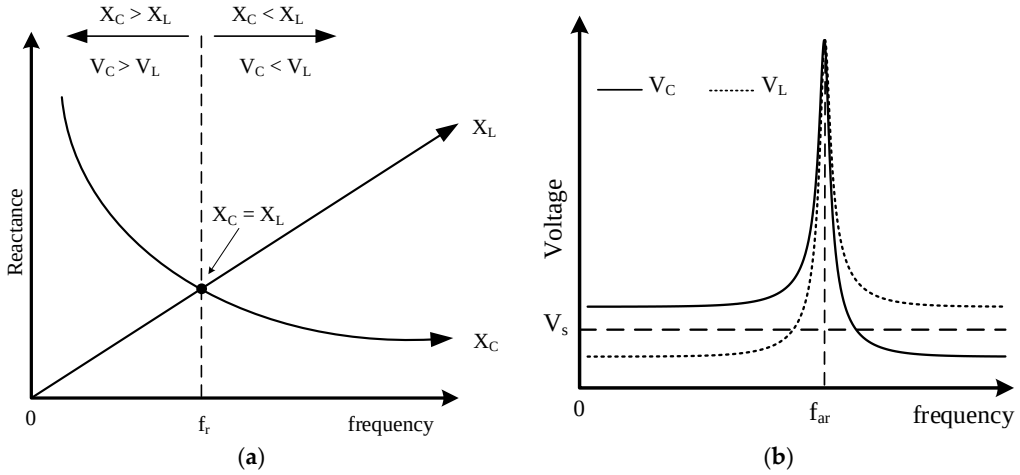
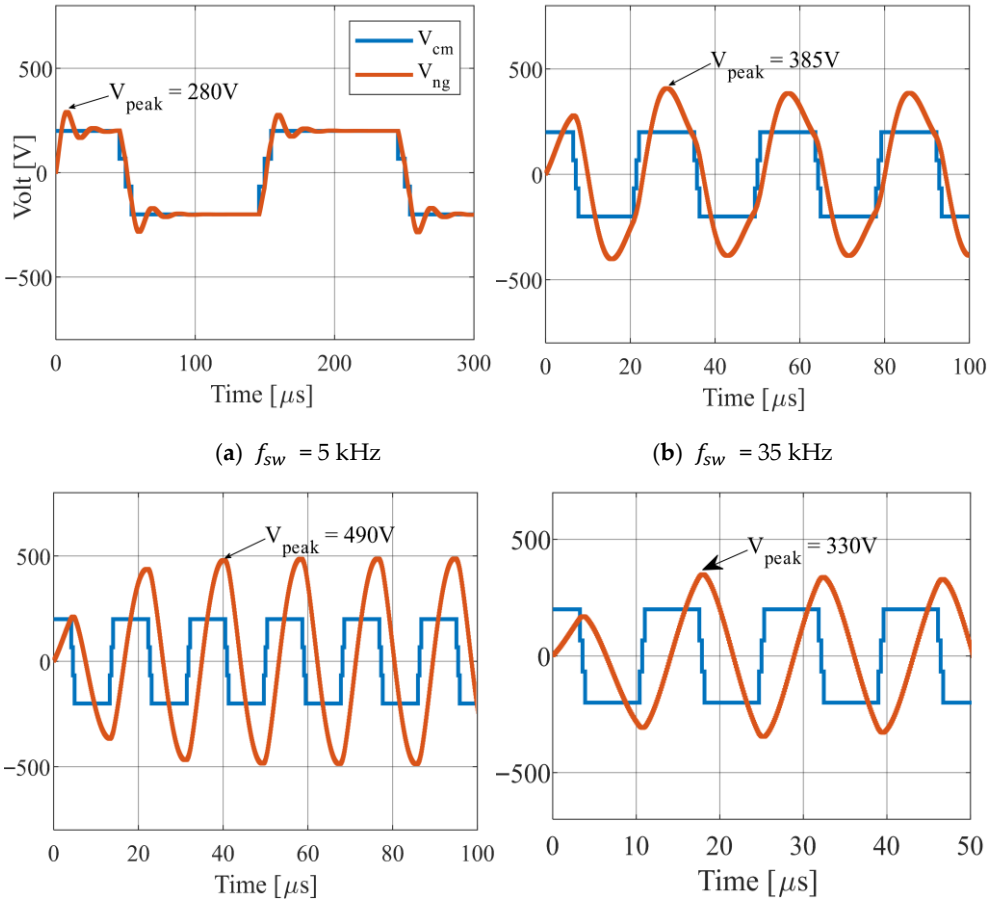



**Figure 3.** Frequency response of a series LC circuit. (**a**) Variation of inductive and capacitive reactance. (**b**) Variation of inductive and capacitive voltage.

By way of example, a motor drive setup is simulated using the motor parameters provided in [7]. The antiresonance frequency $f_{ar}$ of the motor model is 55 kHz. The motor is supplied with a three-phase VSI using conventional SPWM at a dc-link voltage of 400 V and modulation index of 0.3, while the switching frequency $f_{sw}$ is varied. Figure 4 shows the effect of different switching frequencies on motor neutral point voltage. At 5 kHz (see Figure 4a), the $V_{ng}$ exhibits damped voltage oscillations. This oscillatory response arises due to the wave reflection phenomenon, resulting in 1.4 pu (CM voltage peak as base) peak voltage magnitude at the motor neutral point. In subsequent subplots, as the switching frequency increases, the motor neutral point voltage becomes sinusoidal, and oscillation frequency matches the switching frequency. The peak motor neutral point voltage varies non-linearly with switching frequency, where it increases to 1.9 pu when switching frequency approaches machine antiresonance frequency (see Figure 4b) and becomes maximum (i.e., 2.4 pu) when both frequencies coincide (see Figure 4c). However, when switching frequency becomes higher than antiresonance frequency, the voltage decreases to 1.6 pu (see Figure 4d). This demonstrates that the magnitude of motor neutral point voltage depends upon the relationship between switching frequency and antiresonance frequency of the motor.

### *2.2. Effect of Conventional CM Choke Design on Motor Neutral Point Voltage and Bearing Voltage*

Conventional CM chokes are designed to introduce high impedance at targeted frequency ranges (typically in the MHz range) to suppress the EMI. However, incorporating such CM chokes into the drive system increases the overall CM inductance, thereby shifting the CM antiresonance frequency of the motor drive to lower values. These CM chokes are typically used with Si IGBT-based motor drives having practically limited switching frequency of up to 20 kHz, while the motor antiresonance frequency is typically higher than 40 kHz [7]. As a result, although the antiresonance frequency is lowered with CM choke inclusion, it typically remains above the switching frequency. This causes motor neutral point voltage to remain higher than the CM voltage. Nonetheless, the downward shift in motor CM antiresonance frequency may bring it closer to the switching frequency, potentially resulting in an increase in motor neutral point voltage (see Figure 3b).




(**a**) $f_{sw}$ = 5 kHz (**b**) $f_{sw}$ = 35 kHz

(**c**) $f_{sw}$ = 55 kHz (**d**) $f_{sw}$ = 75 kHz

**Figure 4.** Impact of switching frequency on motor neutral point voltage.

As an example, the motor drive simulation model used previously is simulated with and without the conventional CM choke at a switching frequency of 20 kHz. The CM choke inductance is determined based on the CM current profile of the motor drive, as shown in Figure 5a. Without a CM choke, the CM current reaches approximately 75–80 dBμA in the EMI frequency range, which exceeds the permissible limits as described in DO-160F EMI standards (i.e., 72–40 dBμA for 150 kHz–2 MHz and 40 dBμA for 2 MHz–30 MHz) [23]. To meet the standards, a minimum attenuation of 35–40 dBμA is required. Using the insertion loss formula, an attenuation of 35–40 dB corresponds to a CM impedance of approximately 2.8 kΩ at 150 kHz, which converts to a CM choke inductance of 3 mH. Hence, introducing a 3 mH CM choke effectively reduces the CM current harmonics within the EMI range (see Figure 5a). However, the inclusion of the CM choke shifts the motor CM antiresonance frequency from 55 kHz to 40 kHz, as shown in Figure 5b. Although the shifted antiresonance frequency remains higher than the switching frequency, the gap between them is reduced.

Figure 6a,b illustrate the impact of CM choke connection on both the motor neutral point and bearing voltages, respectively. Without a CM choke, the peak neutral point and bearing voltages are 314 V (1.5 pu) and 13 V, respectively. With a 3 mH CM choke, the voltages increase to 357 V (1.7 pu) and 15 V, respectively. This rise in motor neutral point voltage is attributed to the reduced gap between motor antiresonance frequency and switching frequency. Since motor bearing voltage is directly proportional to the neutral point voltage, it increases proportionally. Such a high bearing voltage can cause an electrical breakdown of the motor bearing oil film, producing EDM current spikes. Moreover, a

high neutral-to-ground voltage can also be detrimental to the winding insulation, where it can induce partial discharges that accelerate insulation aging and ultimately result in the degradation of organic coatings on the motor winding.

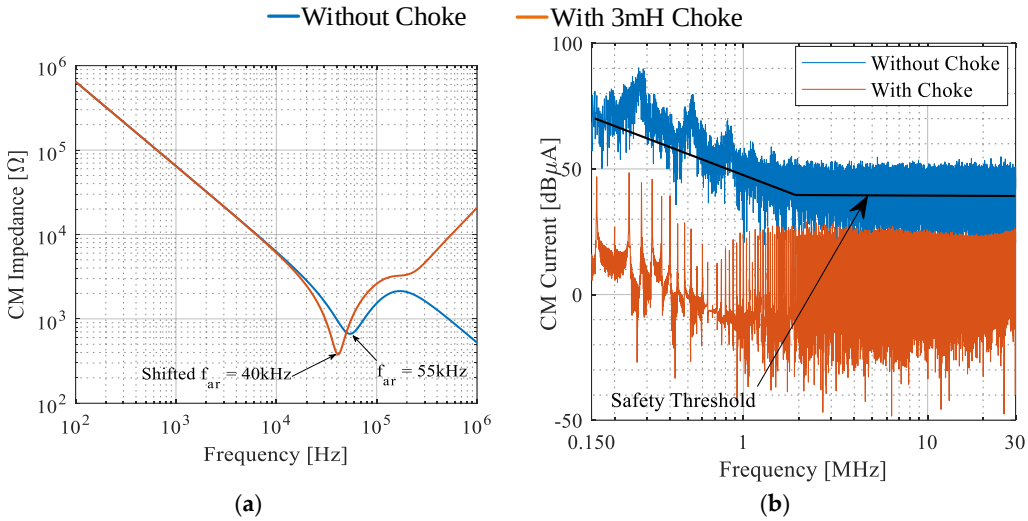



**Figure 5.** Impact of conventional CM choke on (**a**) EMI (**b**) CM impedance.

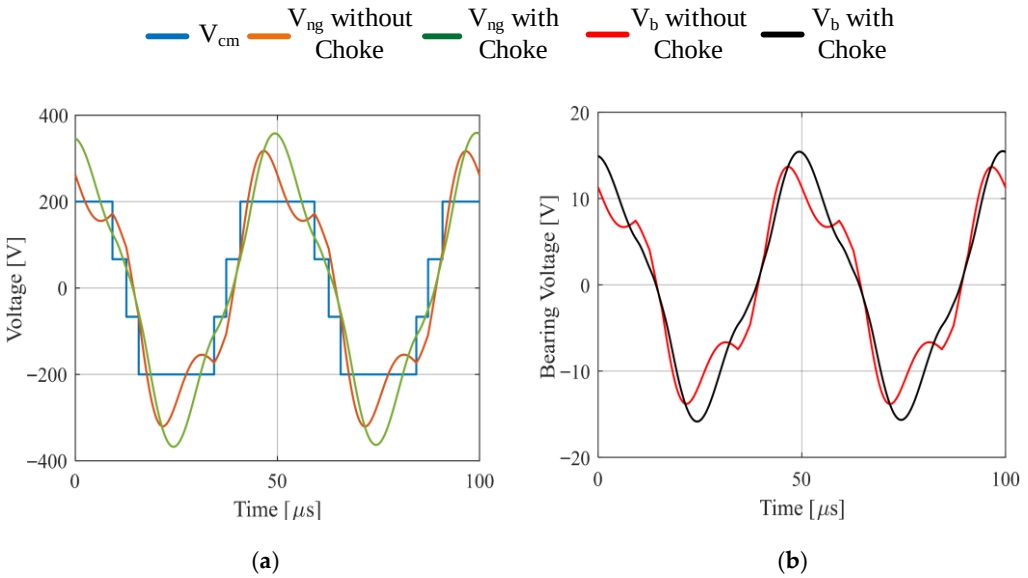



**Figure 6.** Impact of conventional CM choke connection on (**a**) neutral point voltage; (**b**) bearing voltage.

Overall, the conventional CM chokes are effective in attenuating the high-frequency CM current harmonics. However, they do not reduce motor neutral point voltage or its associated adverse effects. On the contrary, their inclusion may increase both neutral point and bearing voltages, thereby posing a significant risk to the motor's lifetime and overall reliability.

## 3. Motor Bearing Voltage and Its Influencing Factors

Bearing voltage, defined as the potential difference between the inner and outer races of motor bearings, has long been recognized as a critical reliability concern in electric motor drives [24]. The adoption of WBG semiconductor devices has further exacerbated its severity, as the higher switching frequencies enabled by WBG inverters intensify neutral point overvoltage. This results in an increase in the dielectric stress across the bearing

lubricant layer, promoting harmful discharge currents that accelerate surface degradation and significantly increase the risk of premature bearing and motor failure.

Electric motors inherently exhibit various parasitic capacitances distributed across different components, including the stator windings, rotor, and bearings. In high-switching-frequency motor drives, these capacitances can provide a low-impedance path, resulting in leakage currents flowing through both the motor frame and the bearings. Furthermore, the winding-to-frame capacitance couples the CM voltage to the motor frame, creating the motor neutral-point potential relative to ground. Simultaneously, the bearing capacitance establishes a capacitive path between the rotor and stator frame, resulting in a voltage difference across the inner and outer bearing races. Figure 7 shows the cross-sectional view of a three-phase star-connected motor, highlighting the different parasitic capacitances distributed throughout the machine. It also highlights the voltages that arise between different motor components, which contribute to the generation of bearing currents. The parasitic capacitances present within the motor are the capacitance from stator winding to grounded frame $C_{wf}$, stator winding to rotor $C_{wr}$, rotor to grounded frame $C_{rf}$, and bearing capacitance $C_b$. The motor bearing capacitance $C_b$ consists of $C_{b_I}$ and $C_{b_O}$, which represent the capacitances from the inner and outer bearing race to the rolling element (ball), respectively. These inner and outer bearing capacitances combine to form the total bearing capacitance, expressed as $C_b$ (i.e., $C_{b_I} + C_{b_O} = C_b$).

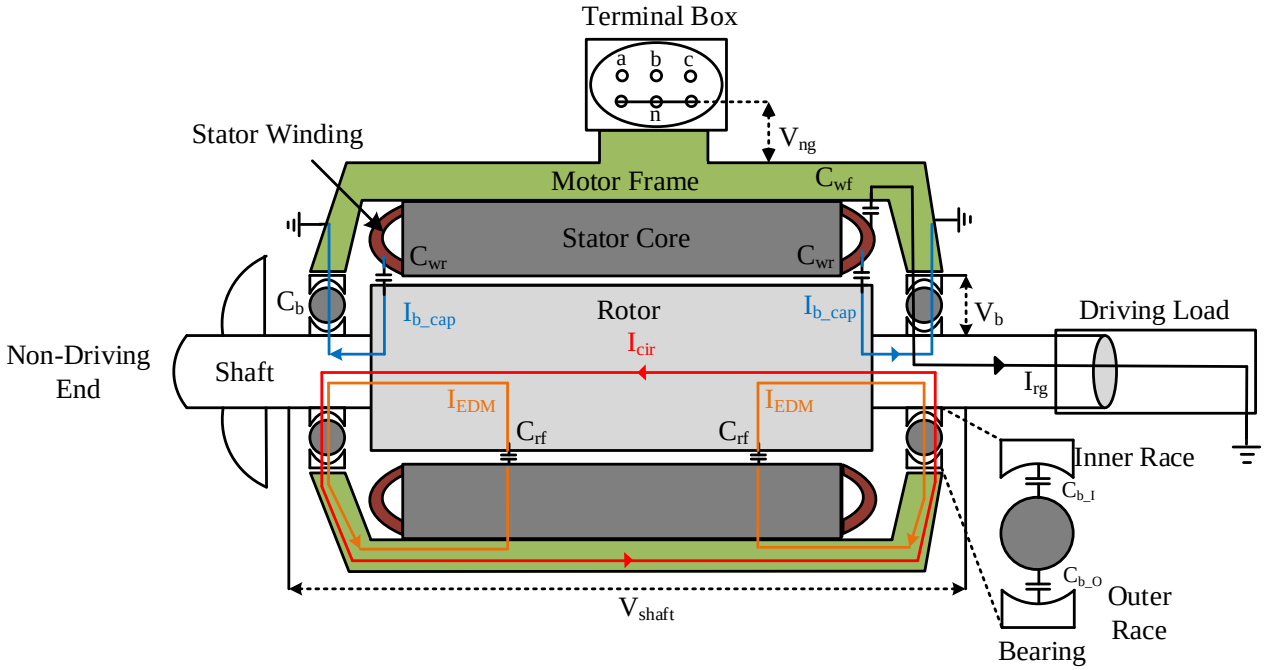


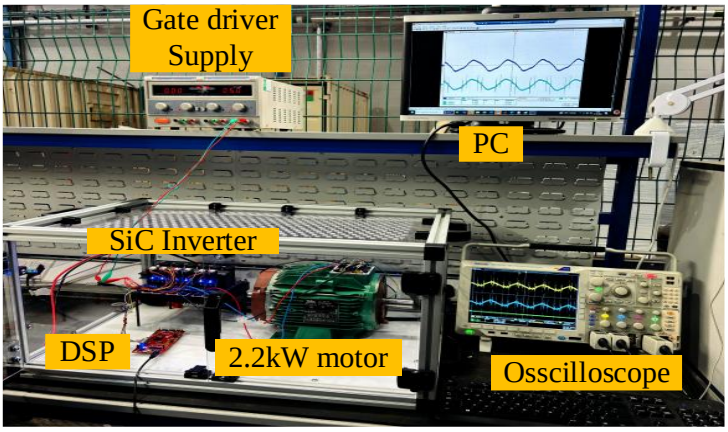

**Figure 7.** Cross-sectional view of a typical three-phase star-connected motor.

In the existing literature, the terms "bearing voltage" and "shaft voltage" are used interchangeably. However, there is a significant difference between the two voltages. The bearing voltage $V_b$ is defined as the potential difference between the inner and outer races of the bearing (i.e., between shaft and grounded frame), while the shaft voltage $V_{shaft}$ represents the potential difference between the driving end and non-driving end bearings [24]. These voltages are directly affected by neutral point voltage $V_{ng}$, which is the voltage between the stator winding neutral point and the grounded frame of the motor, as shown in Figure 7. This voltage is typically assumed to be equal to the inverter CM voltage. However, in the previous section, it was demonstrated that it can be several times higher than the CM voltage, depending on the drive switching frequency. This observation

underscores the need for a detailed investigation into the influence of switching frequency on bearing voltage formation.

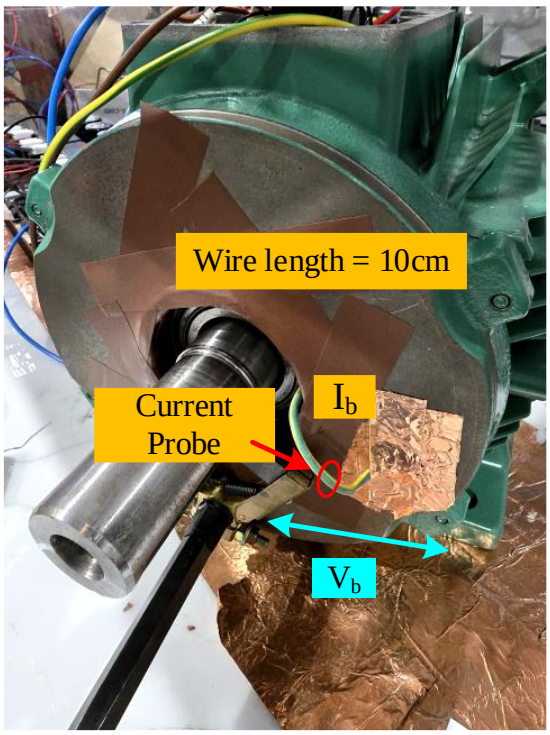
### *3.1. Impact of Switching Frequency*

To observe the effect of switching frequency on bearing voltage, experimental analysis is carried out on a 2.2 kW three-phase four pole star-connected induction motor supplied by a three-phase SiC two-level VSI, as shown in the experimental setup in Figure 8a. Experimental parameters of the inverter, motor, and measurement probes are listed in Table 2. The CM voltage is calculated by averaging the three pole voltages of the inverter, while the neutral point voltage is measured between stator neutral point and grounded motor frame. On the other hand, the bearing voltage is measured between the rotor shaft and ground by using a carbon brush and a V-shaped brush holder, as shown in Figure 8b. The inverter is supplied with a constant dc-link voltage of 600 V at a modulation index of 0.3. The switching frequency $f_{sw}$ is increased from 10 kHz to 60 kHz, and the corresponding effect on $V_{cm}$, $V_{ng}$, and $V_b$ is analyzed. The results are presented in Figure 9, showing how the switching frequency variations impact the motor neutral point voltage and bearing voltage, where they have distinct behaviors, exhibiting peaks that increase/decrease under certain changes in the switching frequency, whereas the CM voltage peak remains constant at 300 V. At low switching frequency, i.e., 10 kHz (see Figure 9a), the bearing voltage and neutral point voltage traverse in different voltage levels almost equivalent to the CM voltage. However, as the switching frequency increases, as shown in subsequent subplots of Figure 9, $V_{ng}$ and $V_b$ become almost sinusoidal due to the increasing filtering effect of motor parasitic capacitances. This again proves that the bearing voltage is directly influenced by the neutral point voltage rather than the CM voltage. Additionally, it can be observed from Figure 10, which summarizes the data collected from Figure 9, that the peak values of both $V_{ng}$ and $V_b$ increase as the switching frequency rises from 10 kHz to 40 kHz, after which these values begin to decrease.




(**a**)

**Figure 8.** *Cont.*




(**b**)

**Figure 8.** Experimental setup. (**a**) Hardware view. (**b**) Bearing voltage and current measurement setup.

**Table 2.** Parameters of Experimental Setup.

| **Inverter Parameter** | **Description** |
|---|---|
| Inverter type | Three-phase VSI |
| Voltage levels | Two-level |
| Switching devices | SiC single N-channel MOSFETs (Wolfspeed C2M0040120D) |
| Switch rating | 1200 V/60 A |
| Gate resistance | 25 Ω |
| Switching rise/fall time | 52 ns/34 ns |
| DSP | TMS320F28379D |
| Modulation technique | Sinusoidal PWM |
| **Motor Parameter** | **Description** |
| Rated line voltage | 400 V |
| Rated line current | 4.9 A |
| Rated Power | 2.2 kW |
| Rated rotor speed | 1445 RPM |
| **Measurement** | **Description** |
| Voltage measurement | 200 MHz Tektronix (THDP0200) voltage probe |
| Current measurement | 120 MHz Tektronix (TCP0030A) current probe |
| Oscilloscope sampling rate | 200 K/s |
| Oscilloscope edge count threshold | 100 mA |
| Oscilloscope record length | 20 million points |

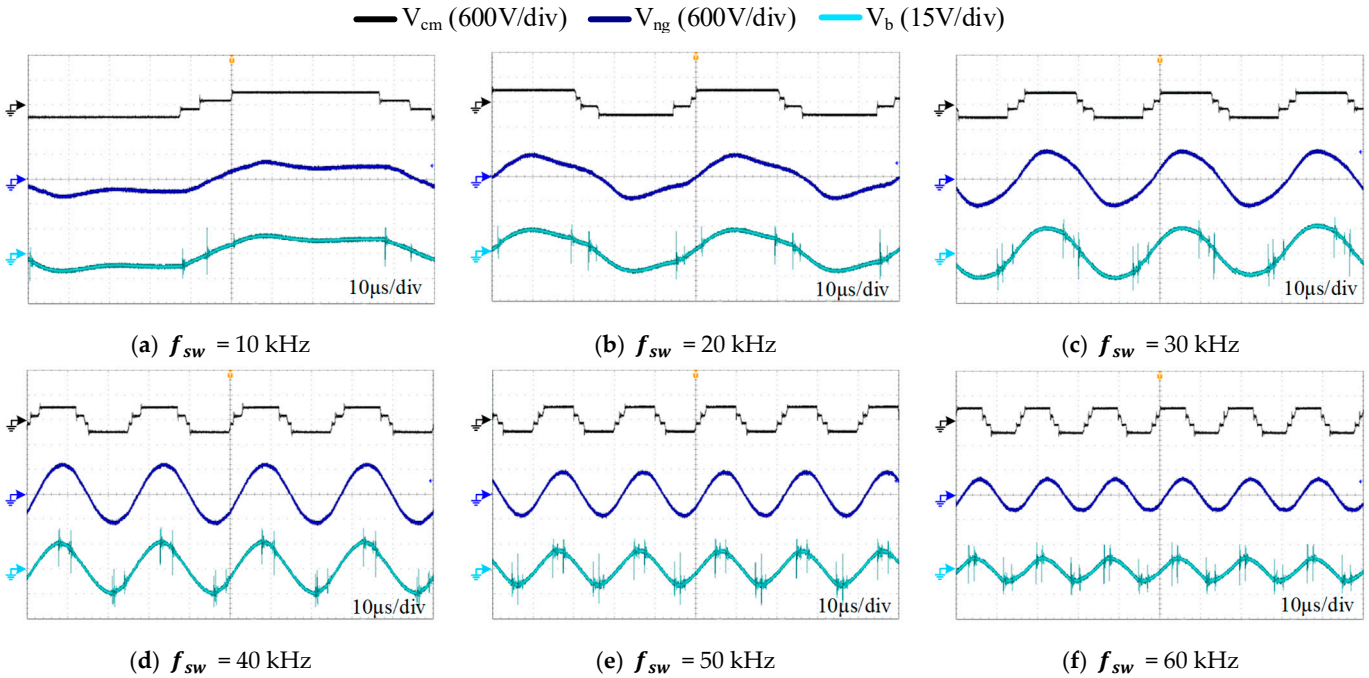



**Figure 9.** Impact of switching frequency on neutral point voltage and bearing voltage.

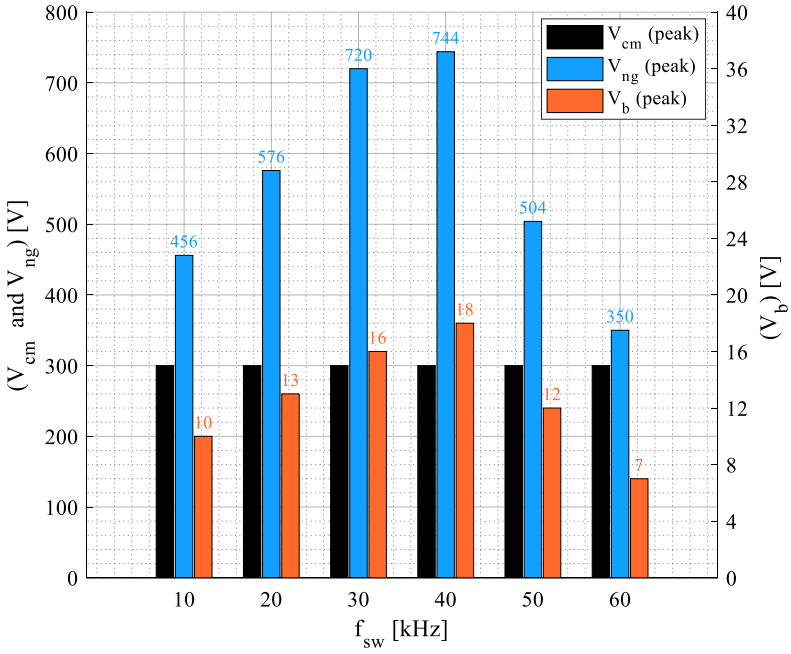



**Figure 10.** Variation in motor neutral point voltage and bearing voltage at different switching frequencies and constant dc-link voltage.

To explain this phenomenon, it is important to consider the machine antiresonance frequency, which can be determined by measuring machine CM impedance between the parallel-connected three phases and ground wire of the motor. To measure the CM impedance of the motor under test, an impedance analyzer Soletron (1260 + 1287) is utilized, and the corresponding CM impedance graph is shown in Figure 11. The machine antiresonance frequency is observed at 41.6 kHz. The motor neutral point voltage, due to its capacitive nature, increases when the switching frequency is below the machine antiresonance frequency (i.e., $f_{sw}$ < 41.6 kHz) (see Figures 9a–d and 10) and decreases when the switching frequency exceeds the antiresonance point (i.e., $f_{sw}$ > 41.6 kHz) (see

Figures 9e,f and 10). A similar trend can be observed in the bearing voltage. The reduction in bearing voltage after the antiresonance point inherently leads to a corresponding reduction in EDM currents, as it is unable to break down the bearing oil film.

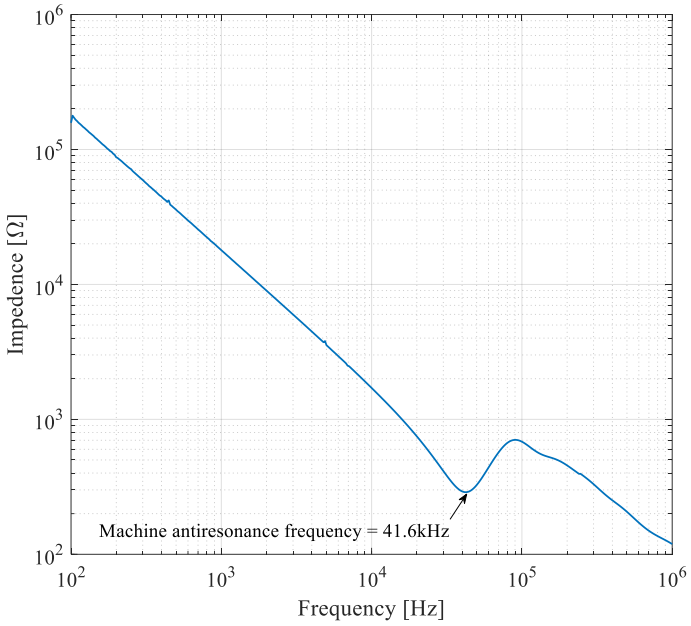



**Figure 11.** CM impedance of the 2.2 kW motor under test.

### *3.2. Impact of Dc-Link Voltage*

To evaluate the effect of dc-link voltage on bearing voltage, the motor drive is operated at a fixed switching frequency of 20 kHz and a modulation index of 0.3, while the dc-link voltage is varied from 200 V to 700 V. The motor neutral point voltage and bearing voltage are measured and illustrated in Figure 12. Furthermore, the peak neutral point and bearing voltage values at different dc-link voltages are summarized in Figure 13. As observed, both the neutral point voltage and bearing voltage are directly proportional to the dc-link voltage. This phenomenon is attributed to the neutral point voltage being derived from the CM voltage generated by the inverter. As the dc-link voltage increases, the CM voltage correspondingly rises, causing an increase in both the neutral point and bearing voltages. At a low dc-link voltage of 200 V (see Figures 12a and 13), the peak neutral point voltage and peak bearing voltage are approximately 195 V and 5 V, respectively (i.e., $V_{ng(peak)}/V_{cm(peak)}$ = 1.95 pu). As the dc-link voltage is increased in the subsequent subplots in 100 V steps up to 700 V (see Figures 12b–f and 13), the neutral point and bearing voltages are observed to increase almost linearly from 195 V to 620 V and 5 V to 15 V, respectively. Since the switching frequency, i.e., 20 kHz, is kept constant at a value far away from motor antiresonance frequency, i.e., 41.6 kHz, the ratio of peak neutral point voltage to peak CM voltage remains almost constant at approximately 1.8–1.9 pu across all dc-link voltages, whereas, in the case of switching frequency matching the machine antiresonance frequency, this ratio was observed as approximately 2.5 pu (see Figure 10). Notably, even at the lowest dc-link voltage of 200 V (i.e., 100 V CM voltage) and a low switching frequency of 20 kHz (away from motor antiresonance frequency), the peak bearing voltage reaches 5 V, which is sufficient to compromise the bearing lubricant film and initiate EDM currents depending upon the bearing geometry and size. Therefore, any mitigation strategy must be designed to consider the influence of dc-link voltage alongside switching frequency to effectively reduce EDM bearing currents.

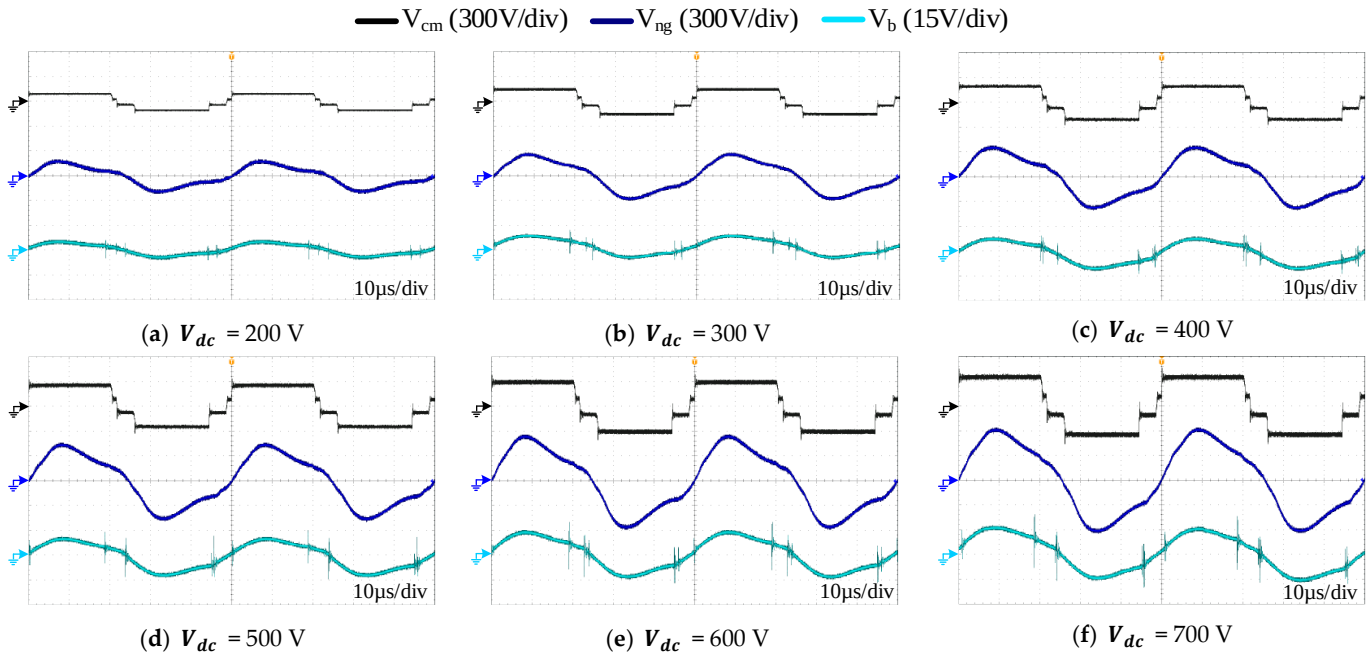



**Figure 12.** Impact of dc-link voltage on neutral point voltage and bearing voltage.

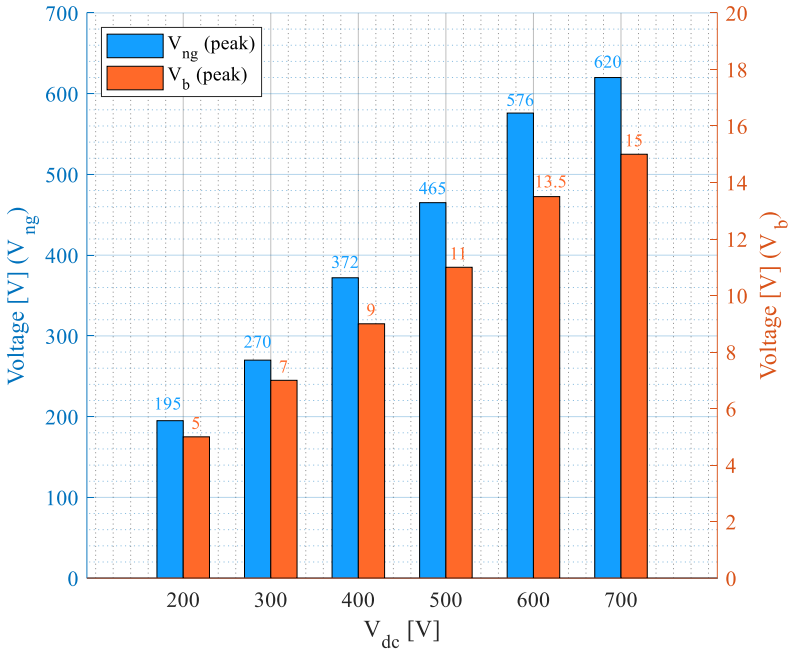



**Figure 13.** Variation in motor neutral point voltage and bearing voltage at different dc-link voltages and constant switching frequency.

## 4. Electrostatic Discharge Machining Bearing Currents

Conventional CM choke designs primarily target the mitigation of CM grounding currents flowing from the stator winding to the grounded motor frame through parasitic capacitances. However, additional grounding currents, known as bearing currents, also exist within the motor. These currents flow from the stator winding to the rotor, and subsequently from the rotor shaft to the grounded motor frame via the motor bearings. In this research, the choke design is specifically focused on reducing bearing currents. An added benefit of the proposed design is its inherent ability to reduce CM grounding currents as well, achieved through the reduction of the motor neutral point voltage and bearing voltage, which acts as the primary driver of CM currents.

Various circulating and non-circulating bearing currents exist within the motor, as demonstrated in Figure 7. High-frequency circulating and EDM bearing currents flow within a closed loop, whereas rotor grounding and dv/dt capacitive bearing currents originate from the motor windings and discharge to the grounded motor frame. The high-frequency circulating bearing current $I_{cir}$ circulates between the stator frame and rotor shaft through the bearings. Similarly, the EDM current $I_{EDM}$ forms a loop beginning at the rotor shaft, traveling through the bearings to the stator frame, continuing to the stator core, and then reaching the rotor core via the capacitance $C_{rf}$ before completing its path back to the rotor shaft. Additionally, a portion of the total CM grounding current may be conducted as rotor ground current $I_{rg}$, particularly when the rotor is grounded through the driven load. On the other hand, the dv/dt capacitive bearing current $I_{b_cap}$ flows from the winding to the rotor, then to the bearing, and finally to the grounded frame through the parasitic capacitances $C_{wr}$ and $C_b$. It is worth noting that the EDM bearing current directly penetrates the lubricating film within the bearing instead of flowing through the bearing capacitances. That is why the EDM current is a primary contributor to bearing degradation compared to the other types of bearing currents.

In the case of healthy lubrication, the bearings maintain lubricant film thickness ranging from 0.1 to 1.4 µm, capable of withstanding voltages between 1.5 and 21 V [25]. However, when this voltage threshold is exceeded, EDM occurs within the motor bearings. This can be visualized by measuring the bearing current of the motor. There are different methods to measure bearing currents, such as direct intrusion measurement, the use of an additional bearing, or radio frequency antenna-based methods. In this paper, a direct intrusive measurement method is employed, as it allows accurate measurement of all types of bearing currents as compared to other methods.

In this method, the motor's endcap is modified to accommodate the measurement circuit, as shown in Figure 14. The motor end cap is widened to incorporate a 1 mm thick metal layer and a 1 mm thick insulation layer. The metal layer is inserted around the bearing, and the insulation layer is positioned between the bearing and the motor frame afterwards to prevent the bearing current from flowing into the motor frame. A short wire is connected to the metal layer and taken out to allow the bearing current to bypass the original internal current flow path, thereby enabling direct measurement of the current passing through the wire. Due to the random occurrence of EDM currents, an "Edge count" function is utilized in the oscilloscope to count the number of EDM spikes. The threshold for EDM current detection is set as 100 mA which is significantly higher as compared to dv/dt bearing currents.

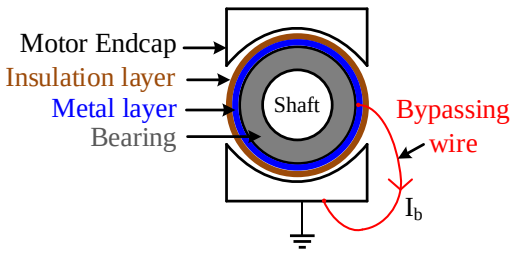



**Figure 14.** Employed bearing current measurement method.

Figure 15 shows the bearing voltage along with the associated bearing current measured at 600 V dc-link voltage and 20 kHz switching frequency. As seen, during the EDM event, the voltage across the bearing drops to zero as the lubricant film ruptures. This rupture causes the energy stored in the rotor-to-frame capacitance to discharge through the bearings, resulting in an impulse current. The released energy generates an arc that can melt the surface of the bearing raceway. The molten material is subsequently rolled

over by the rolling elements, forming a grey trace, and in severe cases, leading to a series of flutings. Some of this molten material may also mix with the bearing lubricant, impairing its insulating properties. Additionally, the rupture of the lubricant creates high temperatures that can cause the lubricant to evaporate. This transient breakdown process lasts only for a few hundred nanoseconds, before which the dielectric lubricant flows back into the gap created by the discharge, reforming a new insulating film. Consequently, the bearing capacitance recharges, and the EDM current ceases. This cycle of breakdown and recovery occurs repeatedly, impacting the bearing voltage waveform after each breakdown. Referring to Figure 15, each time the bearing voltage drops to zero during a breakdown, the voltage waveform shifts upward or downward. A downward shift occurs if the EDM event takes place during the positive half-cycle of the bearing voltage, and vice versa. As a result of this shift, the voltage trajectory deviates from its original path during the subsequent switching event.

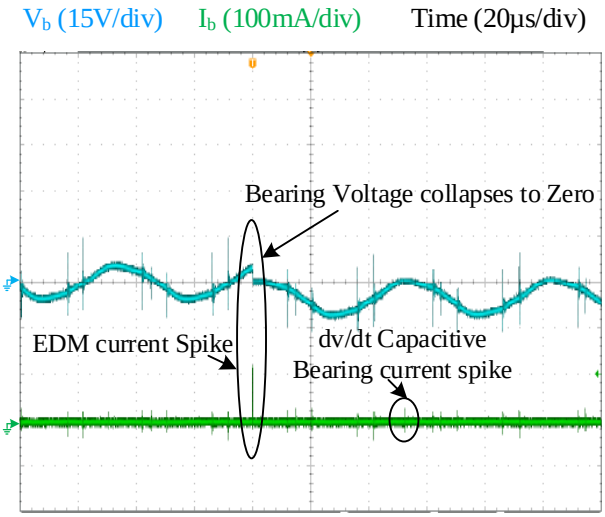



**Figure 15.** Experimental bearing voltage and bearing current waveforms.

On the other hand, the capacitive dv/dt bearing current is generated with each switching event, as shown in Figure 15. The frequency of occurrence of capacitive bearing current is significantly higher than that of EDM current. However, due to its relatively low amplitude (less than 100 mA), this dv/dt bearing current is generally not considered harmful to the bearing raceway. In contrast, EDM currents can range from 200 mA to 1.4 A [26], posing a serious risk of damage to the bearing.

### *4.1. Impact of Switching Frequency on EDM Bearing Current*

To observe the effect of switching frequency on EDM events, the motor under test is supplied by a fixed dc-link voltage of 600 V and a modulation index of 0.3, while the switching frequency is varied from 10 kHz to 60 kHz (10 kHz increment). This switching frequency range is selected to cover the antiresonance frequency of the motor under test (i.e., 41.6 kHz). The results presented in Figure 16 demonstrate that the number of EDM current spikes, within 1 min, rises from 622 at 10 kHz to 1887 at 40 kHz, and then decreases to 146 at 60 kHz. This non-linearity can be explained by considering the machine antiresonance frequency and switching frequency of the drive.

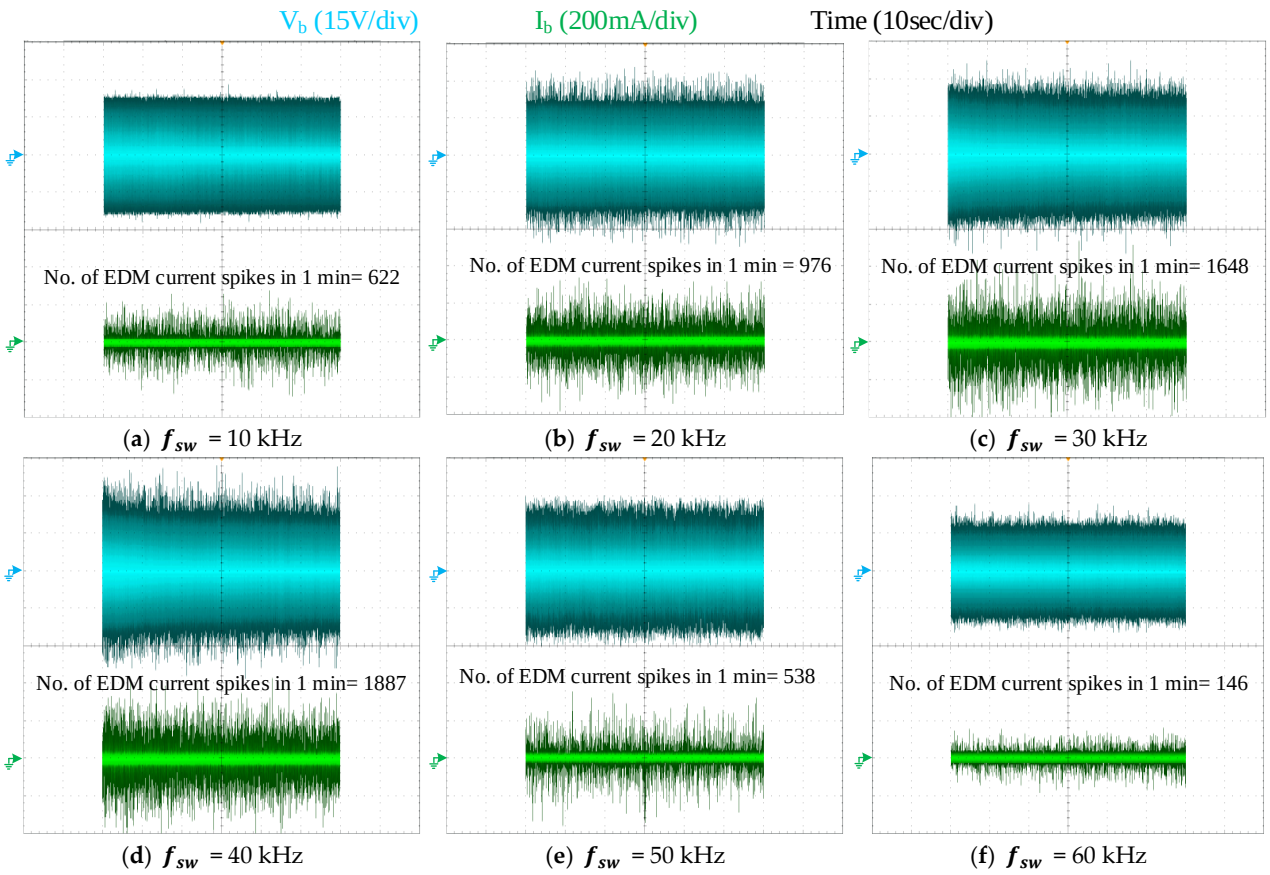



**Figure 16.** Impact of switching frequency on EDM event count.

As demonstrated in Sections 2 and 3, the bearing voltage, which acts as the primary source of EDM current generation, exhibits a direct proportionality to the motor neutral point voltage, whereas the neutral point voltage itself depends on the relationship between the machine antiresonance frequency and switching frequency. Since the antiresonance frequency of the motor under test is measured as 41.6 kHz, the motor neutral point voltage increases when the switching frequency increases up to this antiresonance point.

However, when the switching frequency exceeds the machine antiresonance frequency, the neutral point voltage subsequently decreases. Since the bearing voltage directly reflects the behavior of the motor neutral point voltage, it follows a similar pattern, as demonstrated in Figure 10. Given that EDM current occurrence is governed by the bearing voltage, the increase in switching frequency initially results in an increased EDM current count. Beyond the point where the switching frequency surpasses the machine antiresonance frequency (see Figure 9e,f), the decrease in bearing voltage leads to a corresponding reduction in EDM current events.

### *4.2. Impact of Dc-Link Voltage on EDM Bearing Current*

To evaluate the effect of the dc-link voltage on the EDM current, the motor is supplied at a fixed switching frequency and modulation index of 20 kHz and 0.3, respectively, while the dc-link voltage is varied from 200 V to 700 V in an increment of 100 V. The results presented in Figure 17 show that the number of EDM events, within 1 min, increases from 35 counts at 200 V to 1034 counts at 700 V. This indicates that the increase in dc-link voltage significantly influences the EDM current events, where they increase linearly with increasing dc-link voltage even at low modulation index.

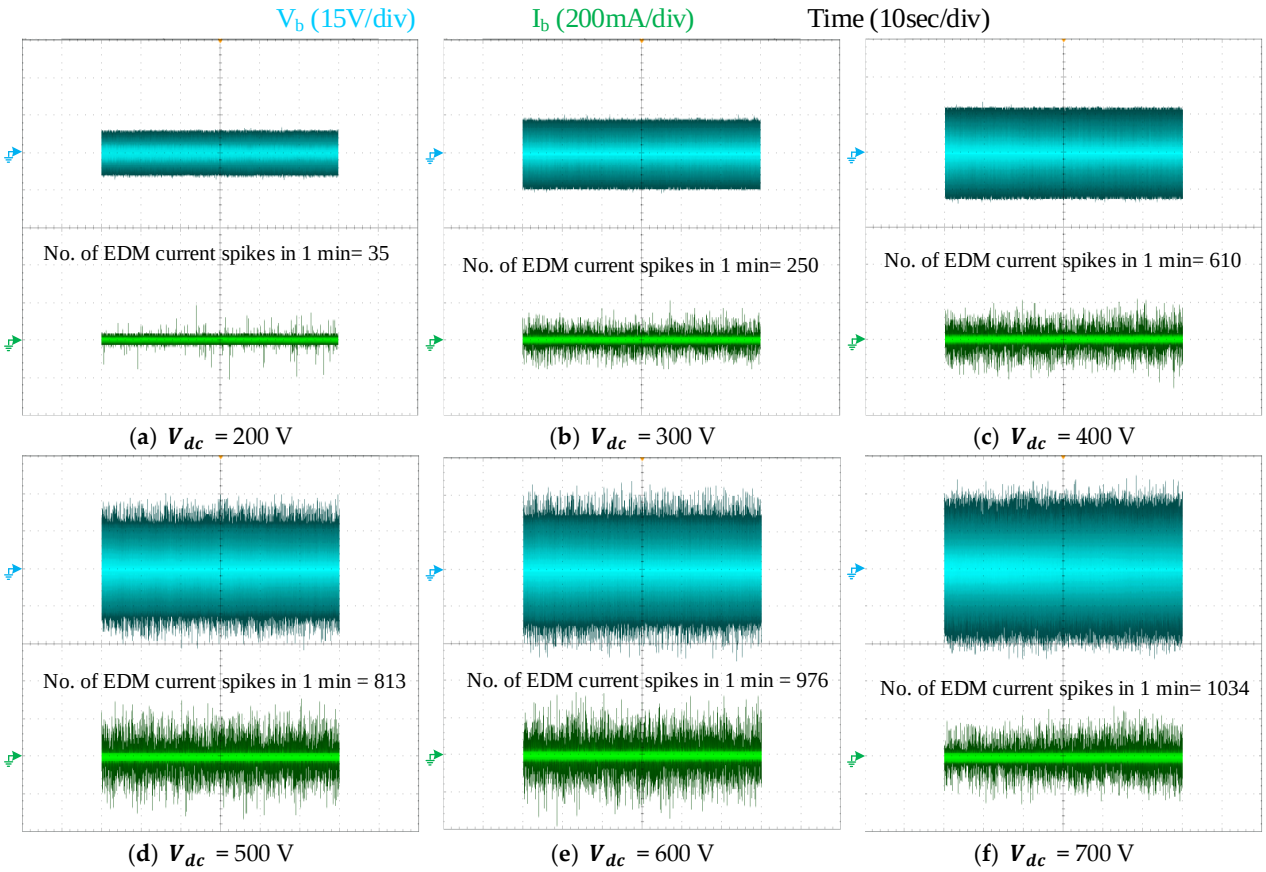



**Figure 17.** Impact of dc-link voltage on EDM event count.

Figure 18 illustrates the combined effects of switching frequency and dc-link voltage on neutral point voltage, bearing voltage, and EDM event count. As shown, the neutral point voltage exhibits a nonlinear variation with switching frequency, attributed to its capacitive behavior, and a linear increase with dc-link voltage, owing to its dependence on the inverter CM voltage (see Figure 18a). Since the bearing voltage and the corresponding EDM current event count depends on motor neutral point voltage, both follow a similar trend with switching frequency and dc-link voltage (see Figure 18b,c), that is, with lower values of both observed at low switching frequencies and dc-link voltages. The values increase progressively and reach a maximum when the switching frequency equals the motor antiresonance frequency (i.e., $f_{sw}$ = 40 kHz) at the highest applied voltage (i.e., $V_{dc}$ = 700 V). Beyond this antiresonance frequency, a further increase in switching frequency results in a decrease in these values, although they remain comparatively high at elevated voltage levels.

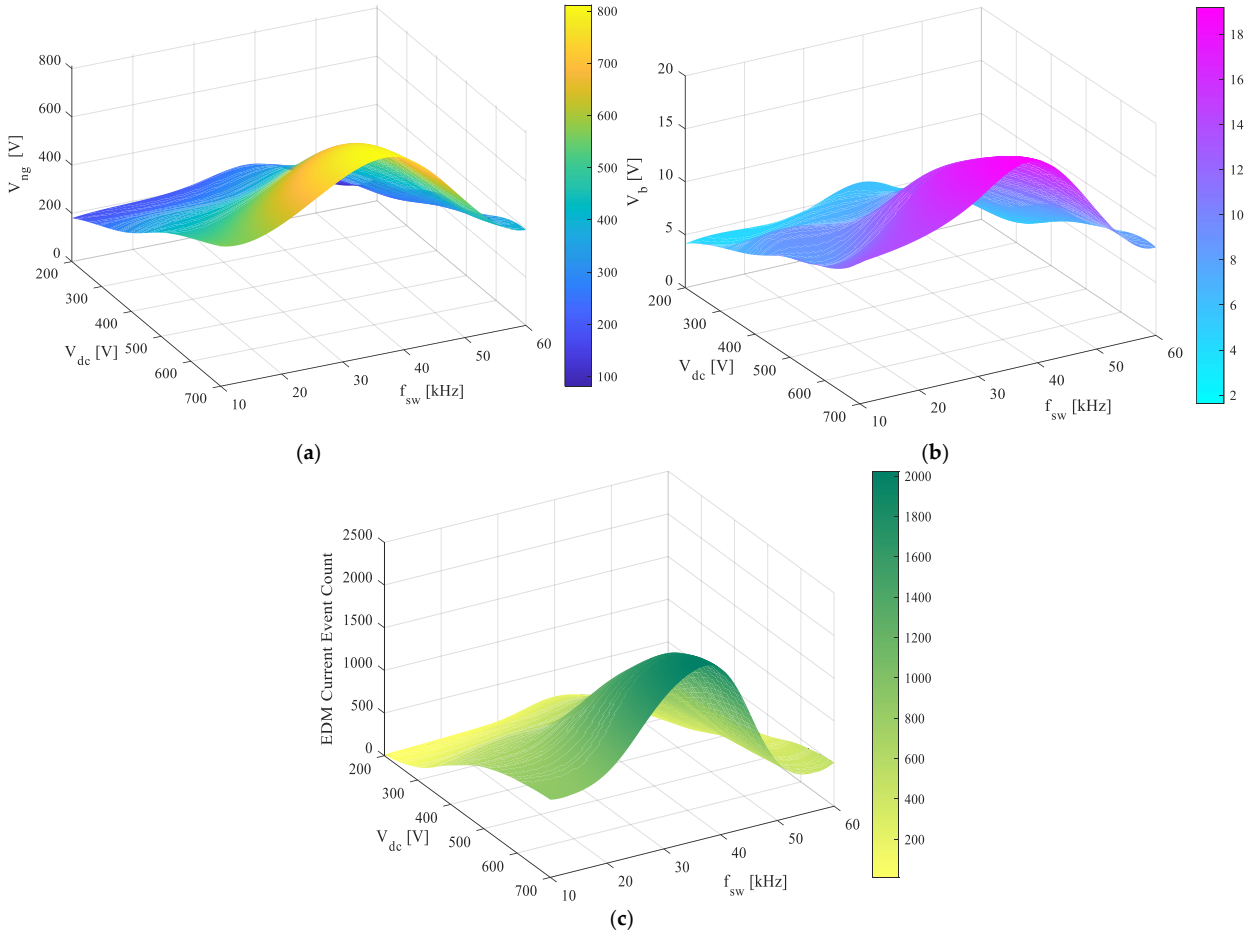



**Figure 18.** Combined effect of switching frequency and dc-link voltage on (**a**) neutral point voltage, (**b**) bearing voltage, (**c**) EDM current event count.

## 5. Proposed CM Choke Design Approach

This paper employs a bearing voltage reduction approach to prevent EDM current events. As outlined in Section 4, when the bearing voltage exceeds the breakdown voltage of the bearing lubricant, the lubricant insulation fails and allows the current to pass through the bearing, resulting in EDM current spikes. To eliminate these spikes, it is essential to reduce the bearing voltage below the lubricant breakdown voltage. As detailed in Section 2, the bearing voltage is directly proportional to the motor neutral point voltage.

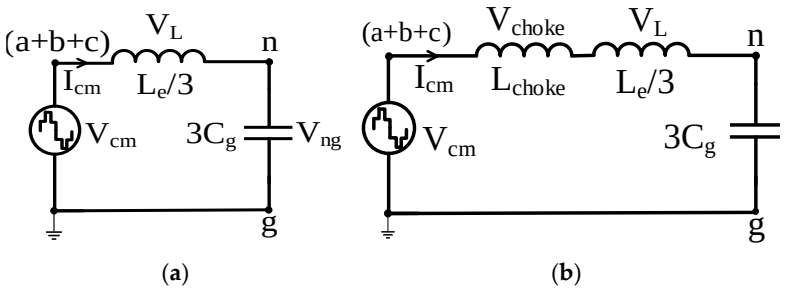
Therefore, reducing the neutral point voltage will inherently reduce the bearing voltage, which decreases the likelihood and magnitude of EDM current generation.

Since the practical switching frequency of IGBT inverters is limited to 20 kHz and motor antiresonance frequencies are typically higher than 40 kHz, the CM chokes conventionally designed for IGBT inverters typically operate under the condition of $f_{sw} < f_{ar_{shifted}}$, where $f_{ar_{shifted}}$ represents the motor antiresonance frequency shifted to lower values due to the inclusion of the CM choke. In this condition, motor neutral point voltage tends to be higher than inverter CM voltage (see Figure 3a,b). Consequently, the conventional CM choke is ineffective at reducing the neutral point voltage and the corresponding bearing voltage. To effectively mitigate these voltages and, in turn, EDM current events, the shifted antiresonance frequency must be lower than the switching frequency, i.e., $f_{ar_{shifted}} < f_{sw}$. Therefore, this paper proposes a CM choke design that optimally shifts the motor antiresonance frequency below the switching frequency, leading to negligible neutral point and bearing voltages, thereby eliminating the EDM bearing current spikes.

### *5.1. CM Choke Inductance Selection*

In this paper, CM choke inductance is determined based on the principle of shifting motor antiresonance frequency to a lower value relative to switching frequency. Referring to Figure 2, the winding-to-frame capacitance is much higher than other parasitic capacitances; therefore, it acts as the dominant capacitance, and other capacitances can be neglected. As a result, the motor CM equivalent circuit shown in Figure 2 can be simplified into a series LC circuit consisting of three-phase equivalent CM inductance $L_e/3$ and equivalent capacitance between neutral point and grounded frame $3C_g$ (i.e., $3C_g = 3C_{wf}/2$), as shown in Figure 19a. According to Figure 19a, the motor antiresonance frequency $f_{ar}$ is given by

$$f_{ar} = \frac{1}{2\pi\sqrt{(L_e/3) \times (3C_g)}} \tag{2}$$




(**a**) (**b**)

**Figure 19.** Motor simplified CM equivalent circuit (**a**) without CM choke connection (**b**) with CM choke connection.

By shifting $f_{ar}$ to a lower value than the switching frequency, the capacitive voltage of the motor CM equivalent circuit (i.e., $V_{ng}$) can be decreased. According to Equation (2), this can be achieved by increasing either $L_e$, $C_g$, or both. Due to the series connection of the CM choke with the motor, its inductance is added to the motor CM equivalent inductance, as shown in Figure 19b. Hence, the total CM inductance increases, effectively shifting the motor antiresonance frequency to a lower value. According to Figure 19b, the shifted antiresonance frequency $f_{ar_{shifted}}$ of the motor, influenced by the series addition of the CM choke inductance $L_{choke}$, is

$$f_{ar_{shifted}} = \frac{1}{2\pi\sqrt{(L_e/3 + L_{choke}) \times (3C_g)}} \tag{3}$$

From Equations (2) and (3), the value of $L_{choke}$ can be calculated as

$$L_{choke} = \frac{f_{ar}^2 L_e}{3f_{ar_{shifted}}^2} - \frac{L_e}{3} \tag{4}$$

where per-phase winding inductance can be determined by rearranging Equation (2) as

$$L_e = \frac{1}{4\pi^2 f_{ar}^2 C_g} \tag{5}$$

Referring to Figure 11, the antiresonance frequency of the utilized motor is observed as 41.6 kHz, whereas $C_g$ can be calculated from the magnitude of CM impedance $Z_{cm}$ in the low-frequency range (i.e., 1 kHz to 10 kHz), as

$$C_g = \frac{C_{wf}}{2} = \frac{1}{6(2\pi f Z)} = 1.35nF \tag{6}$$

where $f$ and $Z$ represent the selected frequency in the low-frequency range and the CM impedance value, respectively. By substituting the determined parameters in Equation (5), the value of $L_e$ for the motor under test is determined as 10.8 mH.

From Equation (4), the value of CM choke inductance required to shift the motor antiresonance frequency to an arbitrary low value can be obtained. However, the optimum shift required in the antiresonance frequency to reduce the bearing voltage to a certain level and eliminate the EDM current spikes requires further calculations.

Motor neutral point can be calculated by applying a voltage divider rule on the CM choke-connected motor CM equivalent circuit shown in Figure 16b. Since the CM choke is designed to reduce the motor antiresonance frequency below the switching frequency, the CM voltage as a function of inductive and capacitive voltage is given as

$$|V_{cm}| = \left|V_{L_{eq}}\right| - |V_{ng}| \tag{7}$$

where ($V_{L_{eq}} = V_L + V_{choke}$). Using the voltage divider rule, $V_{ng}$ can be calculated as

$$\left|V_{ng}\right| = \frac{X_{c_g}}{\left(X_{L_{eq}} - X_{c_g}\right)} \times |V_{cm}| \tag{8}$$

Since the RMS value of CM voltage and the corresponding neutral point voltage varies inversely with the modulation index, the proposed approach is designed for the worst-case scenario where the modulation index is low (i.e., high $V_{ng}$). In the case of lower modulation indices, the three phases switch almost simultaneously. As a result, the inverter CM voltage approximates a square wave, with its RMS value equal to its peak value. Therefore, Equation (8) can be rewritten in terms of peak values rather than RMS values, as

$$\frac{V_{ng_{(p)}}}{\sqrt{2}} = \frac{X_{c_g}}{\left(X_{L_{eq}} - X_{c_g}\right)} \times \frac{V_{dc}}{2} \tag{9}$$

Rearranging Equation (9), the ratio of peak neutral point voltage and peak CM voltage is given by

$$\frac{V_{ng_{(p)}}}{V_{dc}/2} = \frac{\sqrt{2}\,X_{c_g}}{\left(X_{L_{eq}} - X_{c_g}\right)} = k \tag{10}$$

Equation (10) indicates that the motor neutral point voltage can be reduced to any fraction "$k$" of the inverter CM voltage by adjusting the ratio of $X_{c_g}$ and $X_{L_{eq}}$. Substituting $X_{L_{eq}} = 2\pi f_{sw}\,(L_{choke} + L_e/3)$ and $X_{c_g} = 1/\left[2\pi f_{sw}\,(3C_g)\right]$ into Equation (10) and the values of $L_{choke}$ from Equation (4) and $f_{ar}$ from Equation (2) afterwards, the ratio of the shifted antiresonance frequency and switching frequency can be expressed as

$$\frac{f_{ar_{shifted}}}{f_{sw}} = \frac{1}{\sqrt{1 + 1/\sqrt{2}\,k}} \tag{11}$$

Incorporating Equation (11) into Equation (4), the CM choke inductance required to limit he neutral point voltage to any fraction "$k$" of the CM voltage is given by

$$L_{choke} = \frac{\left(1 + 1/k\sqrt{2}\right) f_{ar}^2 L_e}{3 f_{sw}^2} - \frac{L_e}{3} \tag{12}$$

Equation (12) provides the required choke inductance to reduce the peak neutral point voltage to any fraction "k" of the inverter CM voltage. To ensure the elimination of EDM

current, the bearing voltage must be reduced below a critical threshold. Consequently, the value of "k" can be determined based on the required peak bearing voltage level.

From Equation (10), the peak neutral point voltage can be given as

$$V_{ng_{(p)}} = kV_{cm_{(p)}} \tag{13}$$

The peak neutral point voltage can also be calculated using the BVR of the motor given in Equation (1) as

$$V_{ng_{(p)}} = \frac{V_{b_{(p)}}}{BVR} \tag{14}$$

Equating Equations (13) and (14) yields

$$k = \frac{V_{b_{(p)}}}{V_{cm_{(p)}} \times BVR} \tag{15}$$

From Equation (15), the value of "k" can be calculated for any desired peak value of the bearing voltage. The "k" value directly impacts the choke core design and size, specifically the CM volt-seconds impressed on the choke core. The CM volt-seconds can be given as

$$\lambda = \int_0^{\frac{T_{sw}}{2}} V_{L_{choke}}\, dt \tag{16}$$

where $T_{sw}$ is the switchinng period and $V_{L_{choke}}$ is the CM voltage drop across the CM choke, where the value of $V_{L_{choke}}$ can be determined by converting Equation (7) into peak values and substituting the value of $V_{ng(p)}$ from Equation (13) afterwards, as

$$V_{L_{eq}(p)} = (1+k)V_{cm_{(p)}} \tag{17}$$

Assuming a negligible voltage drop across the motor CM winding to emulate the worst-case scenario, the entire CM voltage is dropped across the choke coil. Therefore, $V_{L_{eq}(p)} = V_{L_{choke}(p)}$, substituting the value $V_{L_{choke}}$ in Equation (16) and solving the integration yields

$$\lambda = \frac{(1+k)V_{cm}}{2f_{sw}} \tag{18}$$

To analyze the impact of the fraction "k" on CM volt-seconds, different values of "k" ranging from 0.1 to 1 are substituted into Equation (18), considering switching frequencies of 40, 50, and 60 kHz and a constant dc-link voltage of 600 V. The corresponding CM choke inductances and volt-seconds experienced by the choke core for varying "k" values are shown in Figure 20. As observed, both the required choke inductance and the core volt-seconds decrease as the switching frequency increases. Additionally, lower "k" values require larger choke inductances compared to higher "k" values; however, the volt-seconds across the core are reduced at lower "k" values. Since the volt-seconds are directly proportional to the maximum flux density $B_{max}$ of the core, as expressed in Equation (19), higher "k" values may cause the choke core to saturate, leading to a loss of inductance capability.

$$B_{max} = \frac{\lambda}{nA_e} \tag{19}$$

where $n$ is the number of turns and $A_e$ is the effective cross-sectional area of the core.

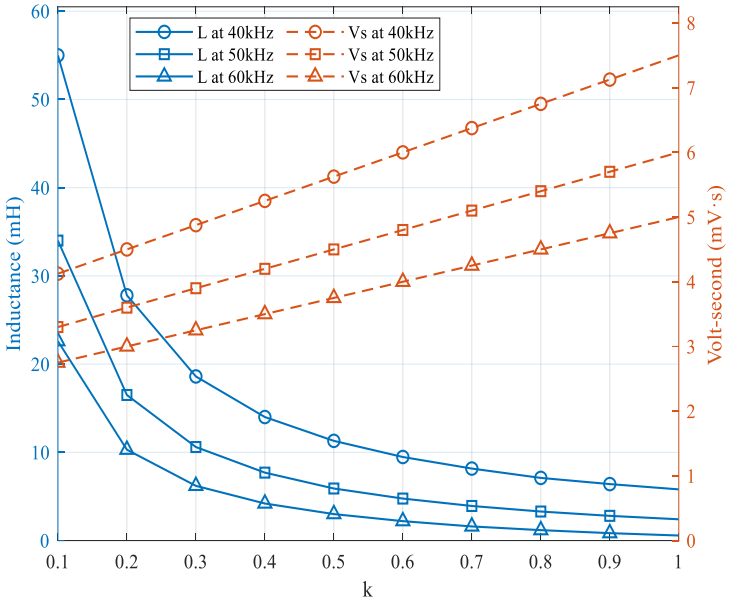



**Figure 20.** Impact of different "k" values on CM choke core volt-seconds.

Furthermore, at higher "k" values, the reduction in choke inductance corresponds to fewer turns, which again increases the maximum flux density and the risk of core saturation. Therefore, to ensure the practical feasibility of the choke size, the "k" value should be kept as low as possible. Although a higher choke inductance will be required at lower "k" values, the size of the choke will remain practical since the core volt-seconds will be lower.

For the motor under test, selecting a peak bearing voltage of $\leq$1 V to fully eliminate EDM currents results in a calculated "k" value of 0.15 using Equation (15), assuming a peak CM voltage of 300 V and the BVR of the motor as 2.2% (calculated based on the peak values of neutral point voltage and bearing voltage). Based on this "k" value, the required choke inductance at a switching frequency of 40 kHz is calculated as 37 mH using Equation (12).

### *5.2. CM Choke Core Selection*

In this paper, the CM choke is designed to shift the motor antiresonance frequency below the switching frequency, resulting in nearly all the inverter CM voltage being dropped across the CM choke. Consequently, the primary concern is the core's ability to withstand the source CM voltage for a period determined by switching frequency. Therefore, to select the appropriate CM choke core, it is important to first calculate the CM volt-seconds across it.

To ensure that the selected choke core is capable of withstanding maximum voltage stress, a worst-case operating condition is assumed. First, the CM voltage drop across the motor winding inductance is considered negligible (i.e., $V_L \approx 0$), such that the entire inductive CM voltage is imposed across the choke. Additionally, a low modulation index is assumed, representing a scenario in which an RMS CM voltage equal to its peak value (i.e., $V_{dc}/2$) is continuously applied across the choke within a switching cycle. Under these assumptions, given a switching frequency of 40 kHz and dc-link voltage of 600 V, CM volt-seconds across the CM choke core can be calculated for k = 0.15 as $\lambda = 4.31$ m Vs using Equation (18).

Furthermore, a nanocrystalline core material with a saturation flux density $B_{sat}$ of 1.2 T–1.3 T is selected. Therefore, the maximum flux density $B_{max}$ in the core is selected to be less than 1.2 T. According to Equation (19), to prevent core saturation, the product of $n$ and $A_e$ must be greater than or equal to $\lambda / B_{max}$. Therefore, by substituting the values for the maximum flux density and maximum volt-seconds into Equation (19), and considering

the number of turns as 40, the cross-sectional area of the core should be larger than 0.89 $cm^2$. Furthermore, determining the inner and outer diameters of the core requires the calculation of the magnetic path length $l_m$, which can be derived from the CM choke inductance as

$$l_m = \frac{n^2 A_e}{L_{choke}} \tag{20}$$

where $\mu = \mu_0 \mu_r$. For nanocrystalline materials, the relative permeability $\mu_r$ is approximately 30,000, yielding a total permeability $\mu = 3.77 \times 10^{-2}$ H/m. Substituting the calculated values into Equation (20), the magnetic path length can be determined as 14.5 cm. Using the values of $A_e$ and $l_m$ and considering the height of the core as 20 mm (for practicality), the inner and outer diameters of the CM choke core are determined as 41 mm and 50 mm, respectively.

The calculated dimensions indicate that the CM choke can effectively withstand 115% of the inverter CM voltage at $V_{dc}$ of 600 V and switching frequency matching machine antiresonance frequency, even at low modulation index. The resulting CM choke size is practical, and a suitable core can be readily selected from commercially available options.

In this paper, a nanocrystalline (Magnetec NANOPERM M-011, $50 \times 40 \times 20$ $mm^3$) core is selected that achieves a volumetric power density of approximately 8–12 kW/L, which is within the same order of magnitude as advanced traction inverters that integrate planar EMI filters, where system-level power densities of 25–35 kW/L have been reported [27,28]. The high saturation flux density (≈1.3 T) and low-loss properties of the nanocrystalline material enable a 30–50% reduction in volume compared with ferrite equivalents while maintaining thermal stability and magnetic headroom. Although the material cost (≈USD 3–25 per core) is higher than that for ferrites, it is justified by the compactness, reliability, and EDM-current suppression that improve drivetrain durability. Therefore, the proposed CM choke offers a practical balance among performance, cost, and volume for WBG inverter-based applications.

### *5.3. Evaluation of Saturation Margin of the Selected CM Choke Core*

The selected nanocrystalline core has a saturation flux density of 1.3 T. The proposed CM choke core is designed to tolerate up to 115% of the CM voltage, resulting in a maximum flux density of 1.18 T. This corresponds to a nominal saturation margin of approximately 9.23%. Although this margin appears narrow, it represents a highly conservative case established to capture worse-case operating conditions. Specifically, the flux density and volt-second stress are evaluated at an extremely low modulation index (≈0), where the CM voltage exhibits its highest magnitude. However, such low modulation indices are not encountered during normal inverter operation.

In practical operation, as the modulation index (MI) increases, the CM voltage transitions from a bipolar square wave to a quasi-square shape; therefore, its effective RMS value decreases, leading to a lower flux swing and greater magnetic headroom. Since no explicit analytical relationship between modulation index and CM voltage RMS is available in the literature, a rough estimation is obtained using MATLAB/Simulink R2022b for a two-level VSI ($V_{dc}$ = 600 V, $f_{sw}$ = 40 kHz). The simulated CM voltage RMS values for modulation indices from 0.1 to 0.9 are then used to compute the corresponding flux linkage (λ), core flux density ($B_{max}$), and saturation margins relative to the nanocrystalline core's saturation flux density.

To emulate transient and surge conditions, a +20% increase in dc-link voltage is applied in all calculations, and the resulting margins are presented in Figure 21. The results indicate that the lowest margin occurs near MI = 0.1, where $B_{max} \approx 1.28$ T (≈1.4% margin). At MI = 0.3, which is the operating point used in this paper, the saturation margin

is approximately 27.5%, even with the 20% surge and 1.15 × $V_{cm}$ stress considered. The margin increases progressively with modulation index, exceeding 80% at M = 0.9.

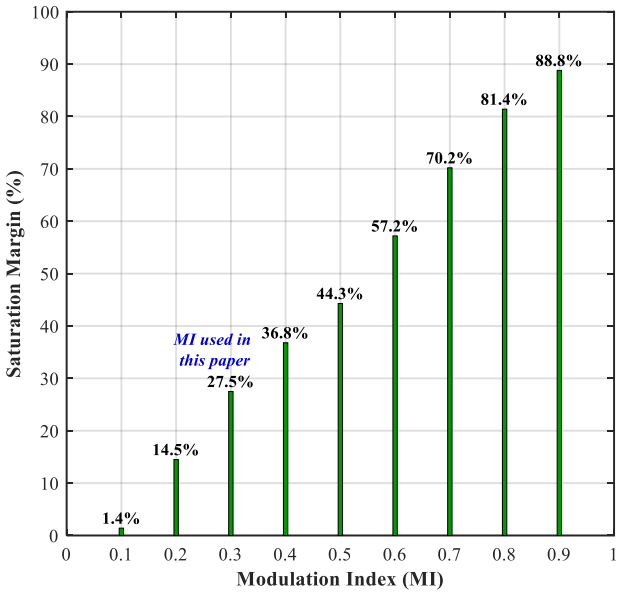



**Figure 21.** Variation of the saturation margin of the proposed nanocrystalline CM choke core with modulation index, considering a 20% dc-link voltage surge.

These results confirm that the choke remains well below the saturation limit under both nominal and transient high-voltage conditions. The corner-case evaluation thus validates that the design is conservative and possesses sufficient magnetic headroom for all expected inverter operating scenarios.

## 6. Experimental Validation

Experimental analysis is carried out on a 2.2 kW three-phase four-pole star-connected induction motor supplied by a three-phase SiC two-level VSI, as shown in the experimental setup in Figure 8. The designed choke and the selected choke core parameters used in the experiment are shown in Figure 22 and Table 3, respectively. The inverter is supplied with a constant dc-link voltage of 600 V at a modulation index of 0.3 and switching frequency of 40 kHz.

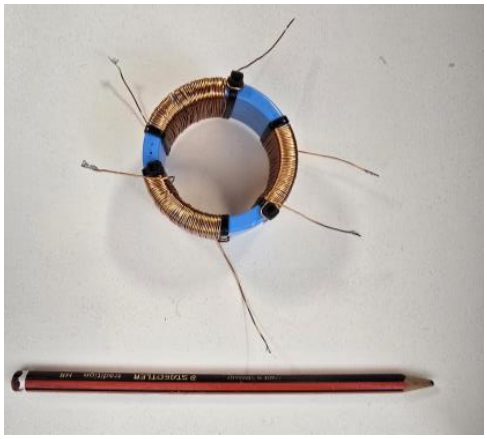


**Figure 22.** A 38 mH choke designed for the experimental analysis, shown alongside a standard pencil for scale.

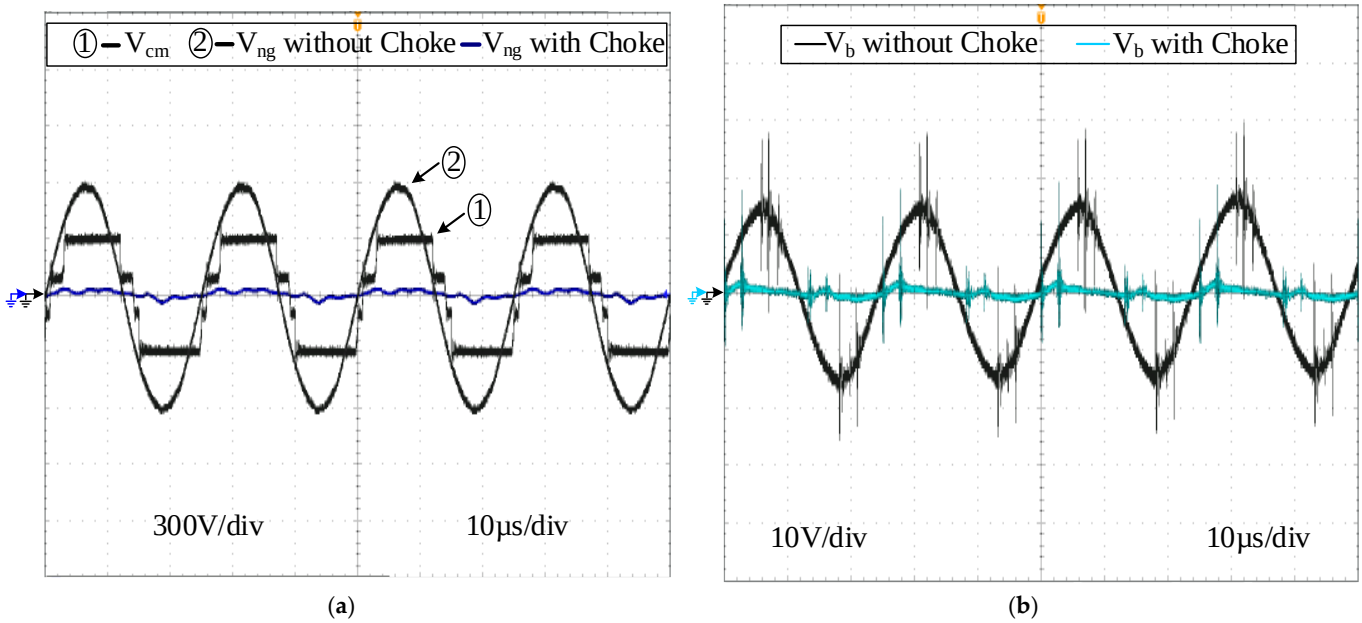
**Table 3.** Calculated and Experimental CM Choke Parameters.

| Designed Choke Parameters | Calculated | Experimental |
|---|---|---|
| Choke inductance | 37 mH | 38 mH |
| Outer diameter | 50 mm | 52.3 mm |
| Inner diameter | 41 mm | 37.1 mm |
| Height | 20 mm | 22.3 mm |
| No of turns | 40 | 44 |

### *6.1. Impact of Proposed CM Choke Connection on Motor Bearing Voltage*

To evaluate the effectiveness of the proposed CM choke in mitigating motor neutral point voltage and resulting bearing voltage, measurements are conducted for both voltages with and without the proposed CM choke connection. On the other hand, the CM voltage is calculated by averaging the inverter pole voltages.

Figure 23 shows the results obtained. As shown, without the CM choke connection, the peak amplitude of the neutral point voltage $V_{ng}$ reaches 600 V (i.e., 2 pu) (Figure 23a), while the peak bearing voltage is observed as 17 V (Figure 23b). Such a high motor neutral point voltage and bearing voltage pose a significant risk to motor winding insulation and bearings. However, with the implementation of the proposed CM choke, the peak neutral point voltage drops to 35 V (i.e., 0.12pu), and the peak bearing voltage drops to 1 V. This substantial reduction in motor neutral point and bearing voltage minimizes electrical stress on motor windings and effectively suppresses the risk of EDM-induced damage to bearings.



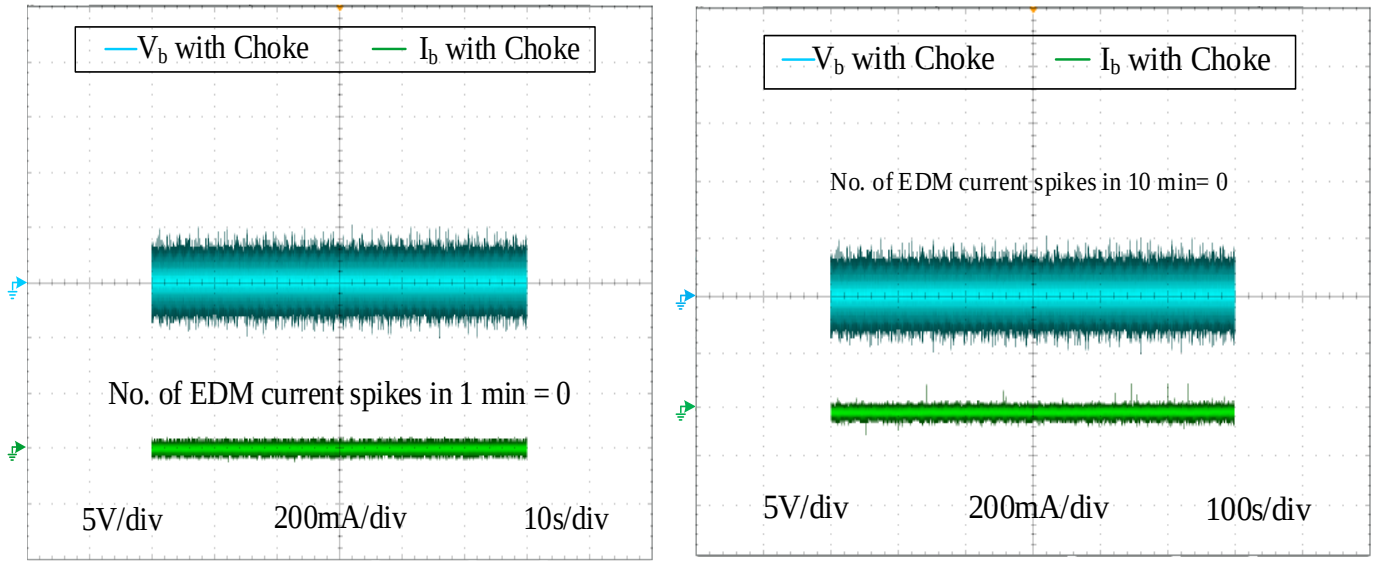

(**a**) (**b**)

**Figure 23.** Impact of proposed CM choke connection on (**a**) neutral point voltage and (**b**) bearing voltage.

### *6.2. Impact of Proposed CM Choke Connection on EDM Bearing Current*

In the case of motor drive operation without any CM choke connected, the highest EDM current count occurred when the switching frequency matched the machine antiresonance frequency, particularly under the high dc-link voltage condition (i.e., at 40 kHz and 600 V) (see Figure 16d). To validate the effectiveness of the proposed approach under these conditions, the bearing current is measured at a switching frequency of 40 kHz, dc-link voltage of 600 V, and modulation index of 0.3 with connection of the proposed CM

choke. The experimental results, presented in Figure 24a, show a complete elimination of EDM current spikes over the specified time frame, whereas 1887 EDM current spikes were recorded in the same time frame when no mitigation was considered.




(**a**) In 1 min (**b**) In 10 min

**Figure 24.** Impact of proposed CM choke connection on EDM bearing current event count.

To further validate the performance of the proposed CM choke, the bearing current is monitored over an extended duration of 10 min, as shown in Figure 24b. It is observed that, with the proposed CM choke connected, no EDM current spikes > 100 mA occur even over the prolonged observation period.

*6.3. Impact of Proposed CM Choke Connection on Motor Common-Mode and Line Current*

To analyze and compare the CM current $I_{cm}$ of the motor drive system with and without the proposed CM choke connection, measurements are taken using a current probe placed across the three lines of the motor (AC side) and around both positive and negative DC buses (DC side). The proposed CM choke lowers the motor's antiresonance frequency relative to the switching frequency, thereby reducing the neutral point voltage, bearing voltage, and the associated EDM bearing current. As the neutral point voltage is the primary driver of CM current, this reduction decreases CM current flow from the motor winding-to-frame/ground (AC side). The CM current, however, circulates in a closed loop: Inverter → Motor windings/parasitics → Motor frame → Ground → DC source/AC mains → Inverter. Hence, any reduction on the AC side inherently leads to a corresponding reduction on the DC side. Thus, the implementation of the CM choke provides simultaneous suppression of CM current on both sides of the inverter.

The results, presented in Figure 25a, show the CM current measured simultaneously on the AC and DC side of the inverter without the CM choke. As shown, the CM current is similar in magnitude as well as waveshape on both sides of the inverter. Furthermore, without the CM choke, CM current exhibits a sinusoidal waveform with high-frequency harmonics and a peak amplitude of 0.9 A, primarily due to the high neutral point voltage. However, with the optimally designed CM choke in place, the CM current is reduced by 83%, lowering the peak amplitude to 0.15 A while also minimizing harmonic content, as shown in Figure 25b. Figure 25c presents the frequency spectrum of the CM current. Notably, with the proposed CM choke, the overall CM current harmonics are attenuated as compared to the case of without the CM choke. Furthermore, in the higher frequency

range (i.e., 10 MHz onwards), it remains around 50 dBµA. Although the proposed choke is designed to eliminate the EDM bearing current, it also attenuates the AC and DC side CM current peak and CM-EMI by reducing the neutral point voltage.

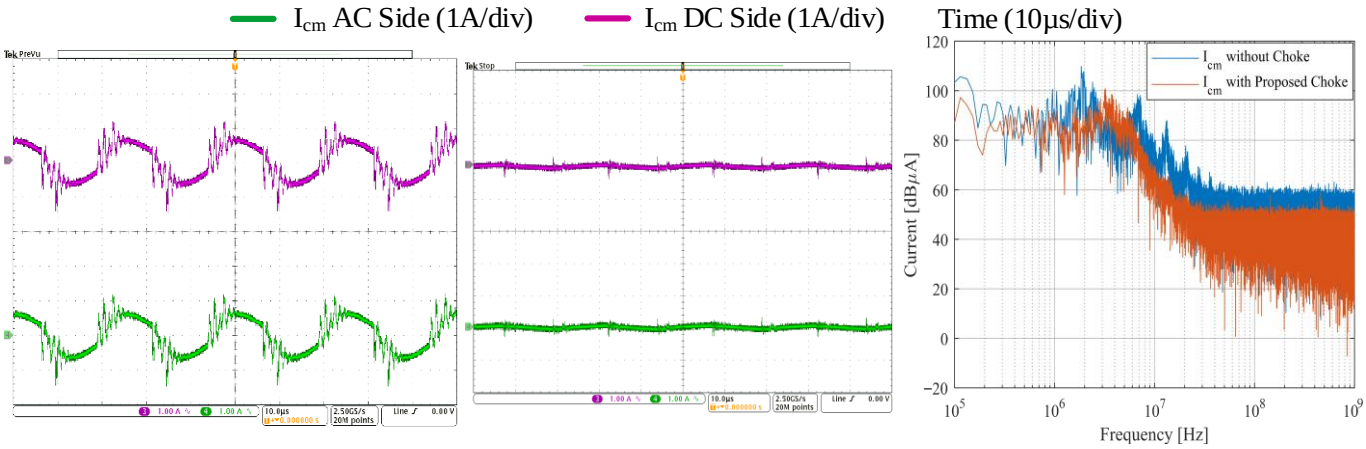



**Figure 25.** Experimentally measured CM current (**a**) without proposed CM choke connection; (**b**) with proposed CM choke connection; (**c**) DC and AC CM EMI.

The line currents also benefit from the proposed CM choke connection, as shown in Figure 26. Without the CM choke, line currents show a peak of approximately 4 A with a noticeable ripple. With the proposed CM choke installed, the peak line current remains almost the same; however, the ripple amplitude is effectively reduced, resulting in a smoother sinusoidal waveform with total harmonic distortion reduced from 13.4% to 5.3%. This demonstrates that the proposed CM choke not only suppresses CM disturbances on both the AC and DC sides but also improves line current quality, enhancing overall system performance.

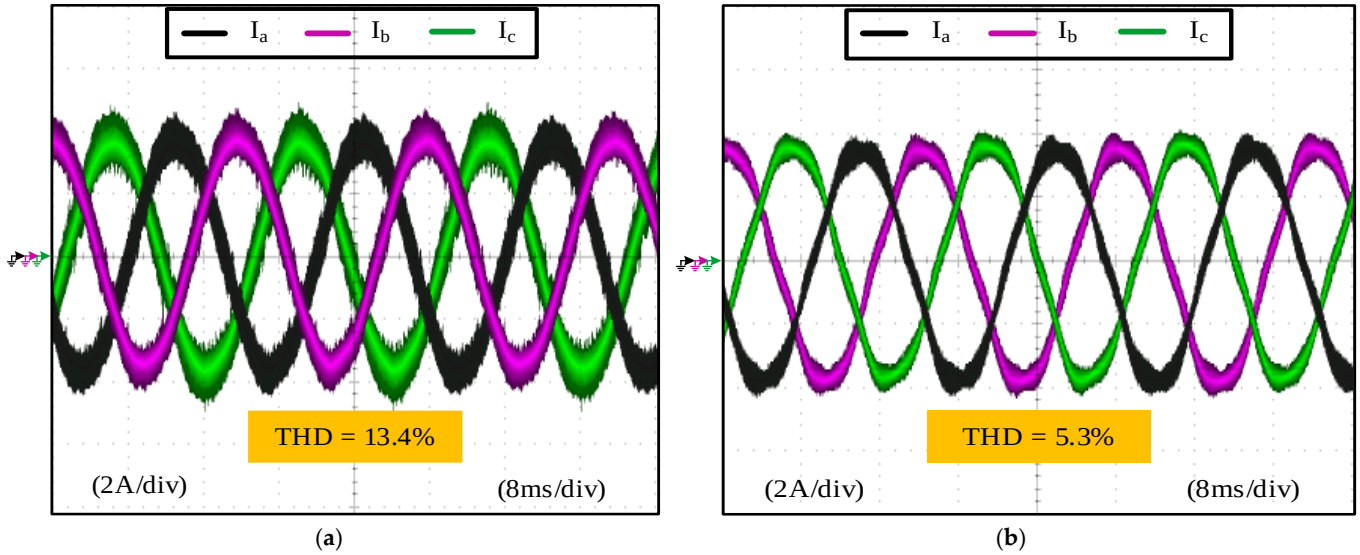



**Figure 26.** Experimentally measured motor line currents (**a**) without proposed CM choke connection; (**b**) with proposed CM choke connection.

Table 4 summarizes the measured impact of the proposed approach on motor parameters in the worst-case scenario. Significant reductions are achieved across all metrics, including a 94% decrease in peak bearing voltage, complete elimination of EDM current spikes, and an 83% reduction in peak CM current. The average EMI level is also lowered

from approximately 85 dBµA to 75 dBµA, indicating improved compliance with EMC guidelines and reduced stress on motor bearings.

**Table 4.** Performance of Proposed CM Choke Design Approach in Reducing Bearing Voltage, Neutral Point Voltage, EDM Bearing Current, CM Current, and Line Current **at** $f_{sw}$ = 40 kHz and $V_{dc}$ = 600 V.

| Parameter | Without Proposed Approach | with Proposed Approach | Percentage Reduction |
|---|---|---|---|
| EDM Current spikes in 1 min | 1887 | 0 | 100% |
| Bearing voltage (peak) | 17 V | 1 V | 94% |
| Neutral point voltage (peak) | 600 V | 35 V | 94% |
| CM current (peak) | 0.9 | 0.15 | 83% |
| EMI (150 kHz–30 MHz) | 110–60 dBµA | 100–50 dBµA | 9–16% |
| Line current | THD = 13.4% | THD = 5.3% | 60% |

### *6.4. Robustness of the Proposed CM Choke Design Under Parasitic Element Variations*

The accuracy of parasitic parameter estimation can be influenced by insulation aging, temperature, and variations among motor designs. Published studies report measured trends in stator insulation capacitance and winding inductance under these conditions, although explicit absolute percentage changes are limited. For example, the Electric Power Research Institute (EPRI) report on thermal aging of stator windings shows that winding-to-frame capacitance changes are typically below 2–3% under moderate deterioration [29]. Thermal-aging experiments on enameled coils indicate similar gradual increases with aging [30], while dielectric measurements on traction-motor winding insulation under thermal aging show a ±1–5% change, with typical operating temperature variations [31]. For the magnetic components, manufacturer data show that permeability variations with temperature can lead to inductance changes of up to ±30%, with typical production tolerances of ±10–20% [32].

Based on these reported trends, a winding-to-frame capacitance variation of up to ±30% and a common-mode winding inductance variation of ±50% is considered for robustness analysis. Figure 27 shows the variation in bearing voltage with the variation in motor parasitic element values. These bearing voltage values are obtained when a fixed proposed CM choke of 37 mH is connected for the worst case of 600 V dc-link voltage and 40 kHz switching frequency. Using the design Equation (12), the "k" values are calculated for each parameter variation and then substituted in Equation (15) to estimate the bearing voltages. As observed in the chart, even with the widest ranges of parameter variations, the peak bearing voltage consistently remains below 3 V, and EDM spikes are unlikely at this small bearing voltage.

To further validate this claim, the motor operating points are adjusted such that, with the proposed 37 mH CM choke, the resulting bearing voltage reaches approximately 3 V (to emulate parameter variation). Under operating conditions of 25 kHz switching frequency, 400 V dc-link voltage, and a modulation index of 0.3, the measured bearing voltage is approximately 3 V, as shown in Figure 28a. Figure 28b shows the corresponding EDM bearing current. As seen, there are no EDM spikes observed even when the bearing voltage increases to 3 V. This confirms that the proposed CM choke design remains resilient to both manufacturing tolerances and operational variability.

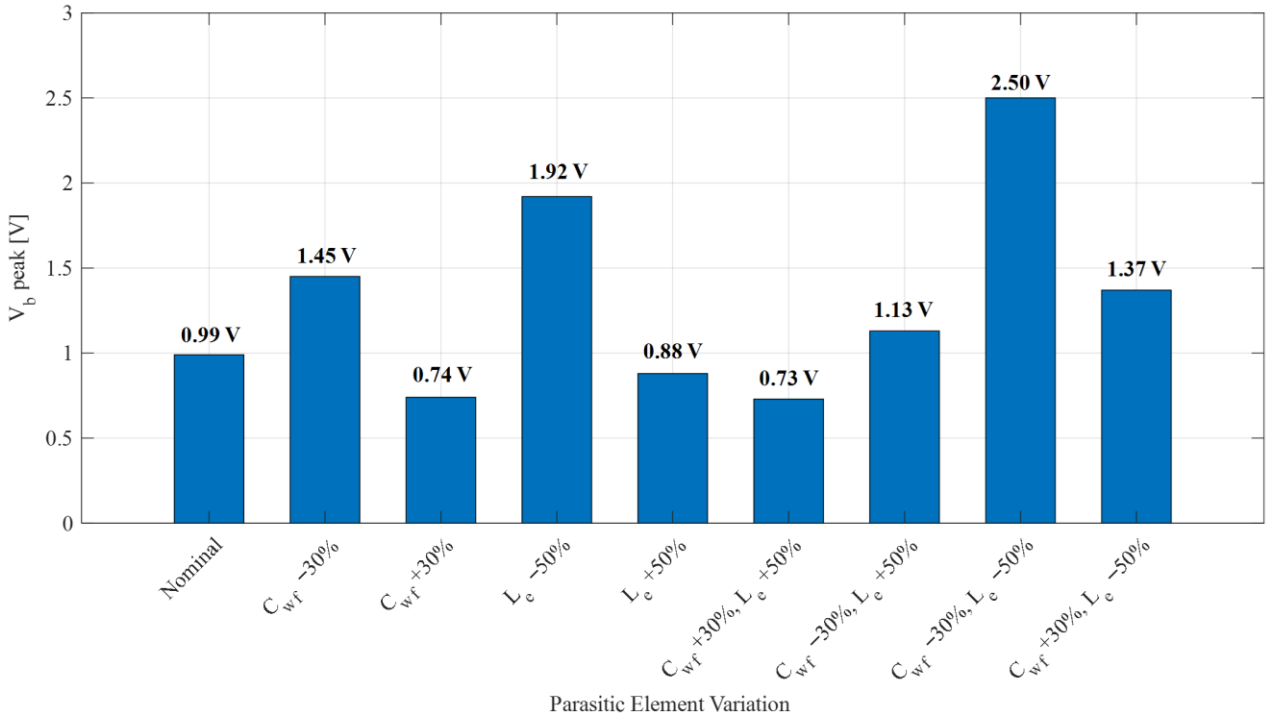
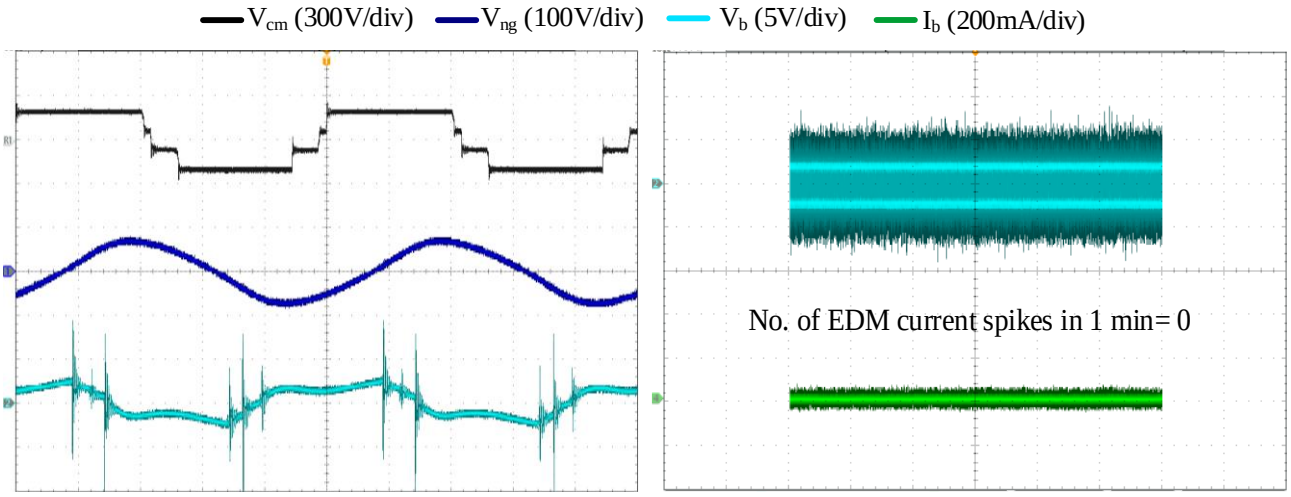



**Figure 27.** Calculated motor bearing voltages for motor parasitic parameter variations.




(**a**) (**b**)

**Figure 28.** Experimental (**a**) motor bearing voltage and (**b**) EDM bearing current measured using fixed CM choke of 38 mH at switching frequency of 25 kHz and dc-link voltage of 400 V.

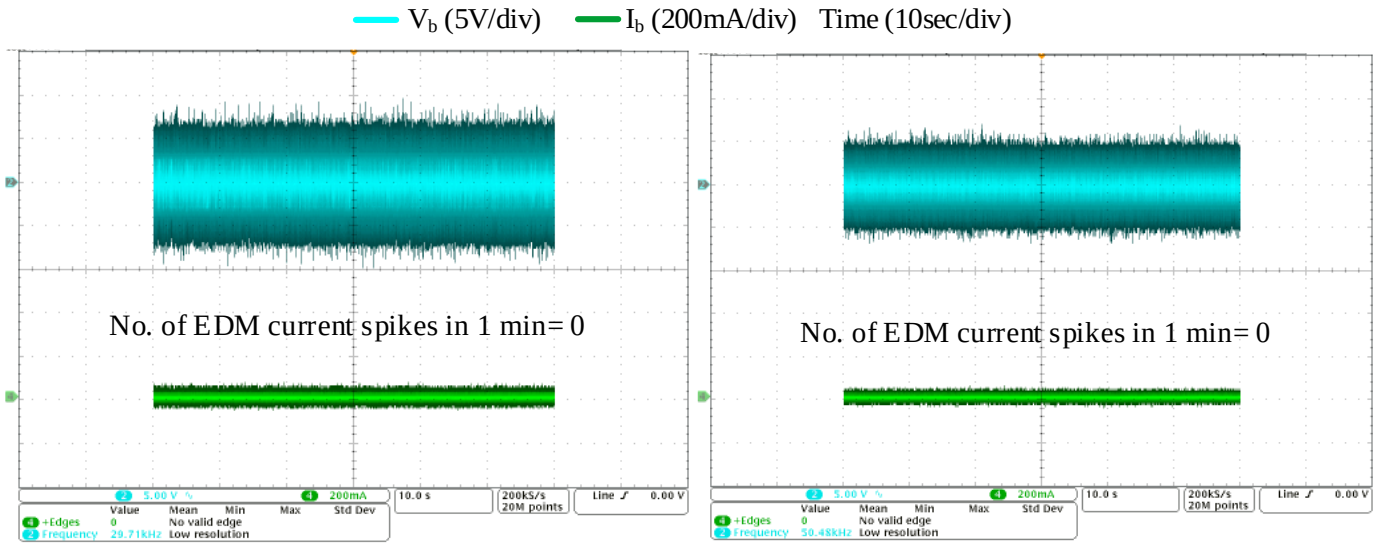
### *6.5. Robustness of the Proposed CM Choke Design Across Different Operating Conditions*

To confirm the robustness of the proposed 37 mH CM choke (designed for switching frequency of 40 kHz) across different converter operating points, additional evaluations are conducted using switching frequencies of 30 kHz and 50 kHz, while all other parameters remain constant. Since the CM voltage, neutral point, and the resulting bearing voltage scale with the dc-link voltage, a lower dc-link voltage inherently reduces these voltages. Therefore, the robustness assessment is carried out at the highest test dc-link voltage of 600 V to represent the most severe operating condition.

The proposed CM choke is analyzed using the design Equation (12) to compute the "k" value for each switching frequency while keeping $L_{choke}$ fixed at 37 mH. The calculated "k" values of 0.29 and 0.09 for 30 kHz and 50 kHz, respectively, are used to estimate the bearing

voltage from Equation (15) and the λ using Equation (18). With a worst-case CM voltage of 300 V and a BVR of 0.022, the resulting bearing voltages are 1.9 V and 0.6 V for 30 kHz and 50 kHz, respectively, while λ varies inversely, being 6.4 mVs at 30 kHz and 3.1 mVs at 50 kHz. Although λ increases slightly at the lower switching frequency, the experimental modulation index of 0.3 reduces the effective CM voltage below 300 V, which compensates for the rise in λ and ensures that both flux and $B_{max}$ remain within the non-saturating limits of the core.

Figure 29 presents the waveforms of the bearing voltage and EDM current measured at different switching frequencies. As shown, across all operating points, no EDM-related discharge spikes occur because the calculated bearing voltage remains below 2 V. These results demonstrate that the proposed single 37 mH CM choke, optimally designed for a switching frequency 40 kHz, exhibits strong robustness across different switching frequencies (higher and lower than 40 kHz). Even under high dc-link voltage, the magnetic stress and bearing voltage remain within safe limits, and no EDM discharge events are observed. Consequently, a single fixed-value CM choke can be confidently applied across a broad operating range, simplifying practical implementation in motor-drive systems.




(**a**) (**b**)

**Figure 29.** (**a**,**b**) Bearing voltage and EDM bearing current at different switching frequencies using fixed CM choke of 38 mH.

### *6.6. Core-Loss Estimation and Thermal Validation of the Proposed CM Choke*

This section presents the analytical estimation and experimental validation of core losses and thermal behavior for the nanocrystalline core employed in the proposed CM choke. The evaluation of the loss characteristics of the Magnetec NANOPERM M-011 material under high-frequency excitation and confirmation the thermal stability of the design under worst-case operating conditions are performed.

The nanocrystalline toroidal core used for the proposed CM choke (Magnetec NANOPERM M-011) is analyzed for core loss and thermal performance under high-frequency excitation. Core losses are estimated using the improved Generalized Steinmetz Equation (iGSE), which accounts for non-sinusoidal flux excitation. Based on the manufacturer's material constants ($k = 2.0 \times 10^{-3}$, $\alpha = 1.45$, and $\beta = 1.95$) at 100 °C, the equivalent coefficient $k_i$ is derived and applied to evaluate the volumetric power loss.

For the applied ±300 V CM voltage (square wave) at 40 kHz and 44 turns per phase, the iGSE model predicts a total core loss of approximately 2.5 W, increasing to 4.9 W

at 60 kHz for a flux swing of 2.4 $T_{pp}$. Thermal analysis based on natural convection (h = 10–20 W/m$^2$K) and the toroid surface area yielded a steady-state temperature rise of 24–48 K, corresponding to a core temperature of 44–68 °C at 40 kHz in a 20 °C ambient environment. Figure 30 shows the experimental infrared thermography under $V_{dc}$ = 600 V and $f_{sw}$ = 40 kHz with a stabilized surface temperature of about 43.3 °C, indicating a loss of 1.2–2.3 W, which is less than the predicted value due to the reduced effective CM voltage (i.e., modulation index of 0.3) used during testing. Overall, the analytical and experimental results confirm low loss levels and thermally stable operation well below the 130 °C limit of the nanocrystalline material. All detailed calculation steps are provided in Appendix A.

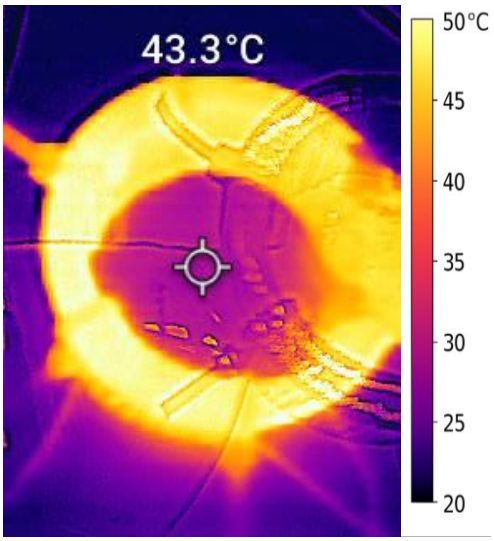



**Figure 30.** Infrared thermography of the proposed CM choke at 600 V dc-link voltage and 40 kHz switching frequency.

### *6.7. Experimental Evaluation of Proposed CM Choke Design Against Existing CM Voltage Reduction Methods for EDM Current Elimination*

Several active CM voltage reduction methods have been proposed in the literature, as discussed in Section 1. While each method employs a different technique, they all share a common limitation in that the maximum achievable CM voltage reduction is constrained to $\pm V_{dc}/6$. This reduced CM voltage is typically sufficient to eliminate EDM spikes at low switching frequencies. However, WBG inverters enable motor drives to operate at higher switching frequencies, increasing the possibility of switching frequency approaching the machine antiresonance frequency. This can excite machine resonance, resulting in a significant overvoltage at the machine neutral point. As the bearing voltage is directly proportional to the neutral point voltage, it can also increase and exceed the bearing lubrication breakdown threshold, even with the CM voltage being reduced to $\pm V_{dc}/6$. As a result, EDM current spikes can still be observed with reduced CM voltage approaches.

Among the CM voltage reduction methods, the modified PWM schemes, such as the AZSPWM, stand out as the most cost-effective solution. Therefore, the proposed approach is compared with the AZSPWM method to evaluate its effectiveness in eliminating EDM current spikes. For comparison, the motor drive under test is operated under the same proposed approach, effectively eliminating EDM current spikes at all switching frequencies. In contrast, under the AZSPWM1 operating conditions using the AZSPWM1 modulation technique instead of SPWM, measurements are recorded for the inverter CM voltage, motor neutral point voltage, bearing voltage, and bearing current.

Figure 31 shows the experimental results under the AZPWM1 modulation method conducted at a dc-link voltage of 600 V and switching frequency of 40 kHz, while the

modulation index is fixed at 0.3. From Figure 31a, it can be observed that the peak CM voltage is limited to ±100 V (i.e., $\pm V_{dc}/6$). However, despite this reduction, a peak neutral point voltage of 290 V and a corresponding peak bearing voltage of 7 V can be observed. This bearing voltage is sufficiently high, exceeding the lubrication breakdown threshold, causing EDM current spikes (see Figure 31b). As seen, there are 626 EDM current spikes occurring within a 1 min interval, which indicates persistent electrical stress on the motor bearing system. In contrast, the proposed approach demonstrates a complete elimination of EDM current spikes under identical operating conditions, as illustrated in Figure 24.

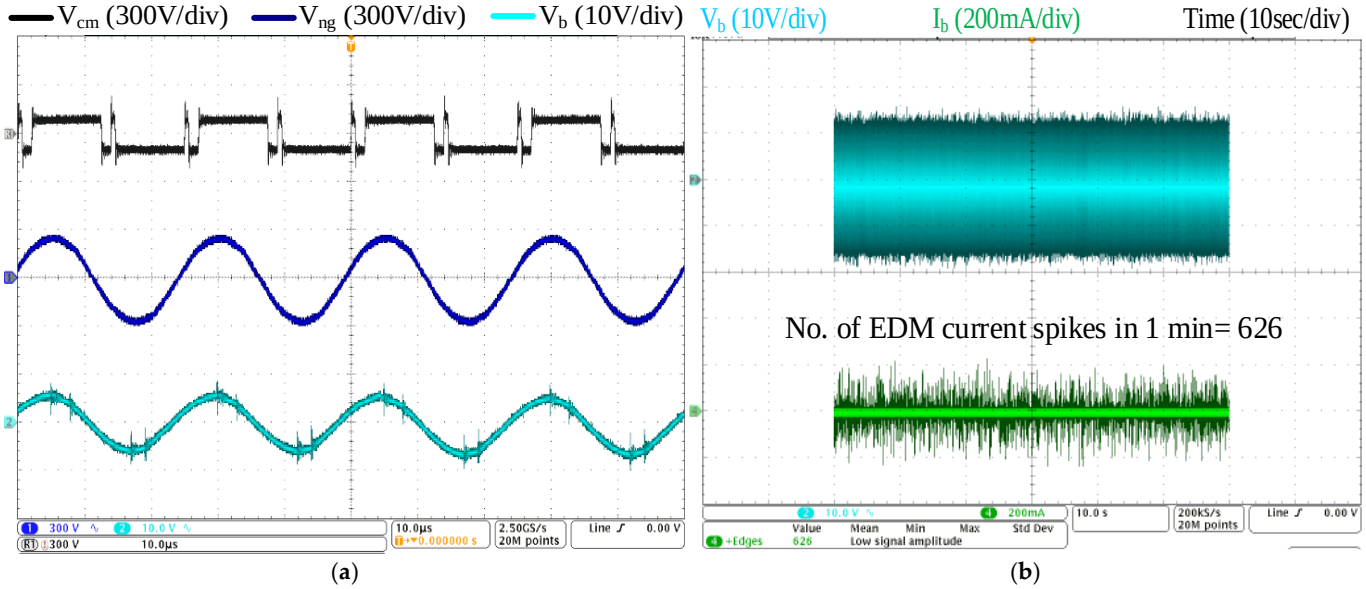



**Figure 31.** Effect of AZSPWM1 modulation technique on (**a**) CM voltage, neutral point voltage, and bearing voltage. (**b**) EDM event count.

## 7. Conclusions

In this paper, a new design approach for a CM choke is proposed. The proposed design overcomes the limitation of conventional CM chokes by effectively eliminating EDM bearing current spikes. Additionally, the proposed CM choke can inherently minimize CM current and EMI by reducing the neutral point voltage. The CM choke inductance is optimally selected to shift the motor antiresonance frequency to an optimized lower value relative to the switching frequency. By maintaining an optimized ratio between these frequencies, the motor bearing voltage can be mitigated, resulting in a complete elimination of the EDM bearing current spikes. Since the proposed CM choke connection shifts the motor antiresonance frequency below the switching frequency, most of the source CM voltage is absorbed by the choke core, thereby minimizing its propagation to the load and bearings. As a result, the CM choke core is specifically designed to withstand the source CM voltage without saturation. The calculations indicate that the CM choke's overall size remains practical, enabling the use of commercially available off-the-shelf cores. To validate the effectiveness of this design, extensive experimental testing is conducted under various operating conditions. The experimental results confirm that the bearing voltage is not only significantly reduced but also maintained below the threshold required for EDM current generation. This ensures that EDM current spikes are eliminated across various operating conditions. The robustness of the proposed approach is experimentally validated, demonstrating the elimination of EDM bearing current spikes under various operating conditions using a single CM choke, without requiring reselection. Furthermore, a comparison of the proposed CM choke with an existing CM voltage reduction technique,

which reduces the CM voltage to $\pm V_{dc}/6$, is performed to assess the relative effectiveness of both methods in addressing EDM bearing currents. This comparison confirms that the proposed CM choke outperforms conventional CM voltage reduction techniques in eliminating EDM bearing currents.

**Author Contributions:** Conceptualization, M.M. and M.D.; Methodology, M.M.; Validation, M.M.; Formal analysis, M.M.; Resources, M.D.; Writing—original draft, M.M.; Writing—review and editing, M.D.; Supervision, M.D. All authors have read and agreed to the published version of the manuscript.

**Funding:** This research received no external funding.

**Data Availability Statement:** The original contributions presented in this study are included in the article. Further inquiries can be directed to the corresponding author.

**Conflicts of Interest:** The authors declare that there are no conflicts of interest.

## Abbreviations

The following terms and symbols are used in this manuscript.

| | |
|---|---|
| $A_e$ | Core cross-sectional area |
| $A_s$ | Core surface area |
| $\alpha$ | Steinmetz exponent (frequency dependent) |
| $\beta$ | Steinmetz exponent (flux dependent) |
| AZPWM | Active Zero State Pulse Width Modulation |
| $B_{max}$ | Maximum flux density |
| BVR | Motor Bearing Voltage Ratio |
| $C_b$ | Bearing capacitance |
| $C_{b_I}$ | Bearing capacitance from ball to inner race |
| $C_{b_O}$ | Bearing capacitance from ball to outer race |
| $C_g$ | Motor parasitic capacitance between neutral point and frame |
| GaN | Gallium Nitride |
| $h$ | Convection heat transfer coefficient |
| $I_b$ | Capacitive bearing current |
| $I_{CIR}$ | High frequency circulating current |
| $I_{cm}$ | Common-mode current |
| $I_{EDM}$ | Electrostatic discharge machining current |
| $I_{rg}$ | Rotor grounding current |
| iGSE | Improved Generalized Steinmetz Equation |
| $k$ | Steinmetz coefficient |
| $k_i$ | Equivalent iGSE constant |
| $l_m$ | Magnetic path length |
| $L_{choke}$ | Choke inductance |
| $L_e$ | Motor winding inductance |
| $\lambda$ | Volt-seconds |
| $m$ | Core mass |
| $N$ | Number of turns per phase |
| $n$ | Number of turns (generic) |
| NSPWM | Near State Pulse Width Modulation |
| $P_{core}$ | Total core loss (W) |
| $P_{meas}$ | Measured power loss |
| $P_v$ | Core loss density (W/kg) |
| $C_{wf}$ | Motor parasitic capacitance between winding and frame |
| $C_{wr}$ | Motor parasitic capacitance between winding and rotor |
| $\Delta B_{pp}$ | Peak-to-peak flux density |
| $\Delta T$ | Temperature rise |
| EDM | Electrostatic Discharge Machining |
| EMI | Electromagnetic Interference |
| EV | Electric Vehicle |
| $f$ | Frequency of excitation |
| $f_{ar}$ | Motor antiresonance frequency |
| $f_{ar_{shifted}}$ | Shifted antiresonance frequency |
| $f_{sw}$ | Switching frequency |
| $V_L$ | Inductive voltage drop |
| $V_{ng}$ | Neutral point voltage |
| $V_s$ | Supply voltage |
| $X_L$ | Inductive reactance |
| $X_{C_g}$ | Motor neutral-point parasitic capacitive reactance |
| $X_{L_{eq}}$ | Motor winding and choke equivalent inductive reactance |
| $Z_{CM}$ | Motor common-mode impedance |

| | |
|---|---|
| $R_{th}$ | Thermal resistance |
| SiC | Silicon Carbide |
| $T_a$ | Ambient temperature |
| $T_{core}$ | Core temperature |
| $T_{sw}$ | Switching period |
| $V_{L_{eq}}$ | Motor winding and choke equivalent voltage drop |
| $V_b$ | Bearing voltage |
| $V_c$ | Capacitive voltage drop |
| $V_{choke}$ | Voltage drop across CM choke |
| $V_{cm}$ | Common-mode voltage |
| $V_{dc}$ | dc-link voltage |
| VSI | Voltage Source Inverter |
| WBG | Wide-Bandgap |
| $X_C$ | Capacitive reactance |

## Appendix A

This appendix provides the detailed calculations used to estimate the core losses and thermal performance of the Magnetec NANOPERM M-011 nanocrystalline core.

**Core Geometry and Excitation Parameters:**

$$A_e = 7.3 \times 10^{-5}\text{m}^2,\ l_e = 0.1403\ \text{m},\ V_c = 1.02 \times 10^{-5}\text{m}^3$$

Material Density = 7250 kg/m$^3$ $\rightarrow$ Core Mass = 0.074 kg.

For the applied excitation conditions ($\pm$300 V CM voltage, $f_{sw}$ = 40 kHz, n = 44 turns per phase):

$$\Delta B_{pp} = 2.4\ \text{T} \Rightarrow B_{max} = 1.2\ \text{T}$$

The rate of flux change is given by

$$\frac{dB}{dt} = 2\, f\, \Delta B_{pp}$$

iGSE Parameters (from datasheet at 100 °C):

$$k = 2.0 \times 10^{-3},\ \alpha = 1.45,\ \beta = 1.95$$

The equivalent iGSE constant is computed as

$$k_i = \frac{k}{\pi^{\alpha-1}} = \left(2.0 \times 10^{-3}\right) / \pi^{0.45} = 8.6 \times 10^{-4}$$

**Loss Density Calculation:**

$$P_v = k_i \left(\frac{dB}{dt}\right)^{\alpha} \left(\Delta B_{pp}\right)^{\beta-\alpha}$$

At 40 kHz:

$$\frac{dB}{dt} = 2\, f\, \Delta B_{pp} = 2 \times 40{,}000 \times 2.4 = 1.92 \times 10^5\ \frac{\text{T}}{\text{s}}$$

$$P_v = 8.6 \times 10^{-4} \times \left(1.92 \times 10^5\right)^{1.45} \times (2.4)^{0.5} = 33.8 \frac{\text{W}}{\text{kg}}$$

Total Core Loss:

$$P_{core} = P_v \times m = 33.8 \times 0.074 = 2.50\ \text{W}$$

Similarly, predicted losses are 3.7 W and 4.9 W at 50 kHz and 60 kHz, respectively.

**Thermal Model:**

The surface area of the toroidal core is approximated as

$$A_s = 0.00524\ \mathrm{m}^2$$

For natural convection (h = 10–20 $\mathrm{W/m^2K}$):

$$R_{th} = \frac{1}{h\ A_s} = 9.5 - 19\frac{\mathrm{K}}{\mathrm{W}}$$

The steady-state temperature rise is given by

$$\Delta T = P_{core} \times R_{th}$$

At 40 kHz:

$$\Delta T = 2.5 \times (9.5 - 19) = 24 - 48\mathrm{K}$$

Hence, for ambient temperature $T_a$ = 20 °C:

$$T_{core} = T_a + \Delta T = 44 - 68\ ^\circ C$$

**Validation:**

Measured core temperature from infrared thermography = 43 °C → ΔT = 23 K.

Back-calculated loss:

$$P_{meas} = \frac{\Delta T}{R_{th}} = 1.2 - 2.3\ \mathrm{W}$$

## References


1. Husain, I.; Ahmed, S.; Qahouq, J.; Rajashekara, K. Electric Drive Technology Trends, Challenges, and Opportunities for Future Electric Vehicles. *Proc. IEEE* **2021**, *109*, 1039–1059. [CrossRef]
2. Zhou, W.; Yuan, X. Experimental Evaluation of SiC MOSFETs in Comparison to Si IGBTs in a Soft-Switching Converter. *IEEE Trans. Ind. Appl.* **2020**, *56*, 5108–5118. [CrossRef]
3. Tesla's Innovative Power Electronics: The Silicon Carbide Inverter. Available online: https://autotech.news/teslas-innovative-power-electronics-the-silicon-carbide-inverter (accessed on 5 August 2025).
4. Diab, M.S.; Zhou, W.; Yuan, X. Evaluation of Topologies and Active Control Methods for Overvoltage Mitigation in SiC-Based Motor Drives. In Proceedings of the 2021 IEEE Energy Conversion Congress and Exposition (ECCE), Vancouver, BC, Canada, 10–14 October 2021; pp. 4867–4873. [CrossRef]
5. Sundeep, S.; Wang, J.; Griffo, A.; Alvarez-Gonzalez, F. Antiresonance Phenomenon and Peak Voltage Stress Within PWM Inverter Fed Stator Winding. *IEEE Trans. Ind. Electron.* **2021**, *68*, 11826–11836. [CrossRef]
6. Memon, M.; Diab, M.; Yuan, X. Mitigation of Machine Neutral Point Voltage in SiC Motor Drives by Controlling Antiresonance Frequency and Switching Frequency. *IEEE J. Emerg. Sel. Top. Power Electron.* **2025**, *13*, 1514–1527. [CrossRef]
7. Schinkel, M.; Weber, S.; Guttowski, S.; John, W.; Reichl, H. Efficient HF Modeling and Model Parameterization of Induction Machines for Time and Frequency Domain Simulations. In Proceedings of the Twenty-First Annual IEEE Applied Power Electronics Conference and Exposition (APEC 2006), Dallas, TX, USA, 19–23 March 2006; p. 6.
8. Han, D.; Morris, C.T.; Lee, W.; Sarlioglu, B. Comparison Between Output Common-Mode Chokes for SiC Drive Operating at 20- and 200-kHz Switching Frequencies. *IEEE Trans. Ind. Appl.* **2017**, *53*, 2178–2188. [CrossRef]
9. Bonnett, A.H.; Yung, C. A Construction, Performance and Reliability Comparison for Pre-EPAct, EPAct and Premium-Efficient Motors. In Proceedings of the IEEE Industry Applications Society 53rd Annual Petroleum and Chemical Industry Conference, Philadelphia, PA, USA, 11–13 September 2006; pp. 1–7.
10. He, F.; Xie, G.; Luo, J. Electrical Bearing Failures in Electric Vehicles. *Friction* **2020**, *8*, 4–28. [CrossRef]
11. Akagi, H.; Shimizu, T. Attenuation of Conducted EMI Emissions from an Inverter-Driven Motor. *IEEE Trans. Power Electron.* **2008**, *23*, 282–290. [CrossRef]
12. Mei, C.; Balda, J.C.; Waite, W.P.; Carr, K. Analyzing Common-Mode Chokes for Induction Motor Drives. In Proceedings of the Power Electronics Specialists Conference (PESC 2002), Cairns, QLD, Australia, 23–27 June 2002; Volume 3, pp. 1557–1562.

13. Muetze, A.; Binder, A. Experimental Evaluation of Mitigation Techniques for Bearing Currents in Inverter-Supplied Drive-Systems—Investigations on Induction Motors up to 500 kW. In Proceedings of the IEEE International Electric Machines and Drives Conference, Madison, WI, USA, 1–4 June 2003; pp. 1452–1457.
14. Turzyński, M.; Musznicki, P. A Review of Reduction Methods of Impact of Common-Mode Voltage on Electric Drives. *Energies* **2021**, *14*, 4003. [CrossRef]
15. Un, E.; Hava, A.M. Performance Analysis and Comparison of Reduced Common Mode Voltage PWM and Standard PWM Techniques for Three-Phase Voltage Source Inverters. In Proceedings of the Twenty-First Annual IEEE Applied Power Electronics Conference and Exposition (APEC 2006), Dallas, TX, USA, 19–23 March 2006; p. 7.
16. Lai, Y.-S.; Chen, P.-S.; Lee, H.-K.; Chou, J. Optimal Common-Mode Voltage Reduction PWM Technique for Inverter Control with Consideration of the Dead-Time Effects-Part II: Applications to IM Drives with Diode Front End. *IEEE Trans. Ind. Appl.* **2004**, *40*, 1613–1620. [CrossRef]
17. Un, E.; Hava, A.M. A Near-State PWM Method with Reduced Switching Losses and Reduced Common-Mode Voltage for Three-Phase Voltage Source Inverters. *IEEE Trans. Ind. Appl.* **2009**, *45*, 782–793. [CrossRef]
18. Guo, X.; Xu, D.; Wu, B. Three-Phase Seven-Switch Inverter with Common Mode Voltage Reduction for Transformerless Photovoltaic System. In Proceedings of the IECON 2014—40th Annual Conference of the IEEE Industrial Electronics Society, Dallas, TX, USA, 29 October–1 November 2014; pp. 2279–2284.
19. Hota, A.; Agarwal, V. A New H8 Inverter Topology with Low Common Mode Voltage and Phase Current THD for Three-Phase Induction Motor Drive Applications. *IEEE Trans. Ind. Appl.* **2022**, *58*, 6245–6252. [CrossRef]
20. Zhou, W.; Diab, M.; Yuan, X. Comparison of Motor Neutral Point Overvoltage Oscillations in SiC-Based Adjustable Speed Drives Using Two-Level and Three-Level Inverters. In Proceedings of the 2022 IEEE Energy Conversion Congress and Exposition (ECCE), Detroit, MI, USA, 9–13 October 2022; pp. 1–8.
21. Ogasawara, S.; Ayano, H.; Akagi, H. An Active Circuit for Cancellation of Common-Mode Voltage Generated by a PWM Inverter. *IEEE Trans. Power Electron.* **1998**, *13*, 835–841. [CrossRef]
22. Turzynski, M.; Chrzan, P.J. Reducing Common-Mode Voltage and Bearing Currents in Quasi-Resonant DC-Link Inverter. *IEEE Trans. Power Electron.* **2020**, *35*, 9553–9562. [CrossRef]
23. *DO-160F*; Environmental Conditions and Test Procedures for Airborne Equipment. Radio Technical Commission for Aeronautics (RTCA): Washington, DC, USA, 2007.
24. Plazenet, T.; Boileau, T.; Caironi, C.; Nahid-Mobarakeh, B. A Comprehensive Study on Shaft Voltages and Bearing Currents in Rotating Machines. *IEEE Trans. Ind. Appl.* **2018**, *54*, 3749–3759. [CrossRef]
25. Abu-Rub, H.; Malinowski, M.; Al-Haddad, K. Common-Mode Voltage and Bearing Currents in PWM Inverters: Causes, Effects and Prevention. In *Power Electronics for Renewable Energy Systems, Transportation and Industrial Applications*; Wiley-IEEE Press: Hoboken, NJ, USA, 2014; pp. 664–694.
26. Tawfiq, K.B.; Güleç, M.; Sergeant, P. Bearing Current and Shaft Voltage in Electrical Machines: A Comprehensive Research Review. *Machines* **2023**, *11*, 550. [CrossRef]
27. Zhao, X.; Hu, J.; Ravi, L.; Dong, D.; Burgos, R.; Chandrasekaran, S.; Eddins, R. Planar Common-Mode EMI Filter Design and Optimization for High-Altitude 100 kW SiC Inverter/Rectifier System. In Proceedings of the IEEE Energy Conversion Congress and Exposition (ECCE), Detroit, MI, USA, 11–15 October 2020.
28. Stella, F.; Vico, E.; Cittanti, D.; Liu, C.; Shen, J.; Bojoi, R. Design and Testing of an Automotive-Compliant 800 V 550 kVA SiC Traction Inverter with Full-Ceramic DC-Link and EMI Filter. In Proceedings of the IEEE Energy Conversion Congress and Exposition (ECCE), Detroit, MI, USA, 9–13 October 2022.
29. Electric Power Research Institute (EPRI). *Testing of Stator Windings for Thermal Aging*; EPRI Report No. 000000000001009252; Electric Power Research Institute: Palo Alto, CA, USA, 2018. Available online: https://restservice.epri.com/publicdownload/000000000001009252/0/Product (accessed on 13 October 2025).
30. Madonna, V.; Giangrande, P.; Galea, M. Evaluation of Strand-to-Strand Capacitance and Dissipation Factor in Thermally Aged Enameled Coils for Low-Voltage Electrical Machines. *IET Sci. Meas. Technol.* **2019**, *13*, 1341–1349. [CrossRef]
31. Gyftakis, K.N.; Sumislawska, M.; Kavanagh, D.F.; Howey, D.A.; McCulloch, M. Dielectric Characteristics of Electric Vehicle Traction Motor Winding Insulation under Thermal Ageing. In Proceedings of the 2015 IEEE 15th International Conference on Environment and Electrical Engineering (EEEIC), Rome, Italy, 10–13 June 2015; pp. 313–318. [CrossRef]
32. Magnetics Inc. *Ferrite Core Catalog 2021*; Magnetics Inc.: Pittsburgh, PA, USA, 2021. Available online: https://www.mag-inc.com/Media/Magnetics/File-Library/Product%20Literature/Ferrite%20Literature/Magnetics-2021-Ferrite-Catalog.pdf (accessed on 13 October 2025).


**Disclaimer/Publisher's Note:** The statements, opinions and data contained in all publications are solely those of the individual author(s) and contributor(s) and not of MDPI and/or the editor(s). MDPI and/or the editor(s) disclaim responsibility for any injury to people or property resulting from any ideas, methods, instructions or products referred to in the content.